

Politecnico di Torino

Communication Engineering
A.a. 2024/2025
Sessione di laurea 10 2025

Space debris detection with LEO satellite constellations

Relatori: Candidates:

Giuseppe Virone Andrea Paternò

Roberto Garello

Sommario

The thesis explores the growing issue of space debris and its implications for satellite operations, insurance, and the sustainability of orbital activities. The accumulation of debris has increased drastically due to the expansion of commercial and governmental use of space, creating a dense and dangerous environment around Earth. Space debris includes inactive satellites, rocket parts, and tiny fragments such as paint flakes or tools lost during extravehicular activities. Even small fragments can pose a severe risk; for instance, a 1 cm object traveling at 10 km/s can destroy a spacecraft. Collisions can result in catastrophic service losses and trigger the Kessler Syndrome, where each impact generates more debris, further elevating collision risks. The main sources of debris are deliberate actions, such as anti-satellite weapon tests and rocket separations, and accidental events like explosions and in-orbit collisions.

Debris is classified by size and altitude. Large debris (>10 cm) can be tracked reliably: medium-sized debris (1–10 cm) is partially trackable, while small debris (1 mm–1 cm) remains beyond detection capabilities. These small fragments, known as lethal nontrackable (LNT) debris, represent 99 % of potential mission-ending collisions. The low Earth orbit (LEO) region is the most crowded, with an estimated probability of one collision every seven years, even excluding untracked objects. Above 650 km altitude, debris-on-debris collisions are more frequent than debris-satellite ones, and in LEO, collision energies are hundreds of times greater than in geostationary orbit. Some satellites can deorbit at the end of their operational life, but many remain uncontrolled, increasing long-term collision risks. Detecting debris relies on parameters such as radar cross section (RCS), object size, and radar configuration. Ground-based radars can detect objects down to 5–10 cm in LEO and larger than 30 cm in higher orbits. Tracking requires repeated observations to determine orbital elements, which are stored in catalogs such as that maintained by the U.S. Space Surveillance Network (SSN). Ground systems like phased-array radars and large parabolic antennas are the foundation of global space situational awareness.

The state of the art in debris detection has expanded from traditional radars and optical telescopes to innovative approaches that leverage existing communication systems. One notable study by Liu et al. proposes using low Earth orbit satellite constellations, such as Starlink or OneWeb, as distributed bistatic radar networks. These constellations use their intersatellite communication links for opportunistic sensing, transforming communication signals into debris detection tools without additional payloads. The method models clusters of debris as correlated scatterers and applies an improved channel estimation algorithm called SAGE2, which operates at the cluster level, reducing computational complexity compared to the standard SAGE algorithm. Simulations using a 14 GHz carrier frequency demonstrated faster convergence and reliable coarse debris localization. This approach offers a cost-effective way to integrate sensing and communication functions in satellite constellations, paving the way for large-scale debris monitoring.

Another significant study by Mahmud et al. focuses on detecting extremely weak Global Navigation Satellite System (GNSS) signals reflected off space debris. These scattered signals suffer from low power and rapidly changing Doppler shifts, complicating detection. The authors propose a multi-stage processing approach that includes correlation, integrate-and-dump filtering, and post-correlation phase correction. By converting the data to an audio-frequency domain, they reduce computational requirements by over two hundred times, while maintaining detection sensitivity. This technique allows long coherent integration (up to 600 seconds), enabling detection of weak reflections without excessive computational cost. It also shows that GNSS signals can be used as passive radar sources for affordable debris tracking.

A complementary method uses laser communication systems for dual-purpose communication and debris detection. The Laser Communications Demonstration Equipment (LCDE) aboard the International Space Station can detect small debris by reflecting a laser beam off its surface. The system measures the time delay and Doppler shift of the reflected signal to determine distance and velocity. Beam divergence and power losses pose challenges, but the use of optical amplifiers and post-correlation processing can significantly enhance sensitivity. This approach highlights the potential of optical payloads for both high-speed communication and precise debris tracking, supporting near real-time situational awareness.

The core part of the thesis evaluates a proposed IRIS2-like satellite constellation for space debris detection. The analysis compares monostatic (same transmitter and receiver) and bistatic (separate transmitter and receiver) radar configurations, including spaceborne satellites (IRIS2-like, MetOp-SG, HY-2) and ground-based systems (TIRA, HUSIR). Debris is modeled as a spherical conductor to simplify the calculation of radar cross section. Depending on the ratio between the debris size and the radar wavelength, three scattering regimes are identified: Rayleigh (small objects), Mie (intermediate), and optical (large objects). For 1 cm debris, the RCS shows oscillatory patterns typical of Mie scattering, while 1 mm debris, in the Rayleigh region, produces a much weaker and smoother response. Detection performance depends heavily on frequency: higher frequencies (Ka-band, around 20 GHz) are needed for sub-centimeter debris.

The radar power budget is evaluated using standard monostatic and bistatic radar equations, considering transmitted power, antenna gains, wavelength, RCS, and target distance. The analysis shows that received power scales inversely with the fourth power of distance in monostatic configurations, and with the square of each path distance in bistatic ones. System noise and bandwidth determine detection thresholds and range resolution. To improve detectability, the study introduces a code enhancement factor through phase-modulated continuous-wave (PMCW) radar using Gold sequences of length 1023. Phase coding reduces sidelobes in the autocorrelation function, resulting in a signal enhancement of about 30 dB. PMCW offers superior range resolution, better Doppler tolerance, and resilience to interference, making it ideal for modern radar systems integrated with communication functions.

Simulations compare several platforms. The IRIS2-like satellite at 1200 km altitude, operating at 12 and 20 GHz with 1 W transmission power, shows limited detection range (only a few kilometers) for 1 mm debris, indicating that this setup is not optimal for LNT detection. The MetOp-SG satellites, operating at 5.2 GHz with 540 W and 39.6 dBi antenna gain, achieve detection up to 330 km for 1 cm debris. The Chinese HY-2 satellites, at 13 GHz and 120 W, provide intermediate results but remain less effective than MetOp-SG. Ground-based radars outperform spaceborne ones. The TIRA radar,

operating at 1.33 GHz with up to 2 MW power and 49.5 dBi gain, can detect 1 cm debris up to 1100 km and 1 mm debris around 230 km. The HUSIR system, operating in X- and W-bands, achieves even higher resolution, imaging objects as small as 5 mm in low Earth orbit.

The findings reveal that while space-based radars are limited by power and antenna constraints, they can still complement ground-based systems through cooperative or bistatic configurations. Integrating LEO constellations with terrestrial sensors could provide continuous and distributed coverage. The use of intersatellite communication links, phase-coded radar waveforms, and shared radar-communication architectures represents a promising direction for future debris detection systems.

In conclusion, the thesis demonstrates that combining ground-based assets like TIRA and HUSIR with LEO constellations such as IRIS2 offers a practical and scalable approach to monitoring small, hazardous debris. Although on-board detection is constrained by power and sensitivity limits, it can serve as an early warning layer within a multi-tiered detection network. Advanced signal processing techniques such as SAGE2, PMCW modulation, and GNSS-based passive sensing enhance detection accuracy and efficiency. These developments mark an evolution toward integrated sensing and communication frameworks, transforming satellite constellations into cooperative sensing infrastructures that can help secure the long-term sustainability of space operations.

Indice

\mathbf{E}	lenco	delle	figure	VIII
1		roducti		1
	1.1	-	debris classification and Distribution	2
	1.2		tability and Trackability Criteria for Space Debris	5
	1.3	Detect	tion from ground	6
2	Sta	te of tl	he Art in space detection	7
	2.1	Debris	s Sensing Based on LEO Constellations: An Intersatellite Channel	
		Param	neter Estimation Approach	7
		2.1.1	Introduction	7
		2.1.2	Conceptual Framework and Motivation	8
		2.1.3	Signal and Channel Modeling	8
		2.1.4	Channel Parameter Estimation: SAGE and SAGE2 Algorithms .	9
		2.1.5	Simulation Setup and Results	9
	2.2	Afford	lable Processing for Long Coherent Integration of Weak Debris-	
		Scatte	ered GNSS Signals with Inconsistent Doppler	11
		2.2.1	Introduction	11
		2.2.2	Proposed Processing Approach	12
		2.2.3	Computational Considerations	12
		2.2.4	Experimental Validation	12
	2.3	Detect	tion of Small-Sized Space Debris Using Laser Communication System	ns 13
3	Spa	ce Del	oris Detection with $IRIS^2$ -like Constellation	16
_	3.1			$\frac{17}{17}$
	3.2		Power Budget and Range Resolution Model	20
		3.2.1	Code Enhancement	22
	3.3	Scenar	rio	27
	3.4		static	28
		3.4.1	$IRIS^2$ -like high	28
		3.4.2	METOP - sg	31
		3.4.3	HY-2	34
		3.4.4	TIRA	35
		3.4.5	HUSIR	37
	3.5		ic setup	39
	-	3.5.1	$IRIS^{2}(highorbit): TX - IRIS^{2}(loworbit) RX \dots \dots$	45
		3.5.2	$MetOp - SG : TX - IRIS^{2}(loworbit) : RX \dots \dots \dots$	46
		3.5.3	$HY2:TX-IRIS^2(loworbit):RX$	48

Bi	bliog	raphy								59
4	Con	clusior								58
	3.6	Results	$CSTR \cdot TX = T$ comparison Optimization	 	 	 				53
			TIRA: TX - IR. HUSIR: TX - I.							

Elenco delle figure

1.1 1.2 1.3 1.4	Damage caused by space debris [1]	1 2 3
0.1		_
2.1 2.2	Scenario kind for sensing based on LEO	7
2.2	dashed lines are TX1-RX, TX2-RX, TX2-RX	10
2.3	Comparison with conventional SAGE: iteration time	10
2.4	Direct and Scattered GNSS signal	11
2.5	Link Scheme	14
3.1	Constellation and Ground RADAR considered for the analysis	17
3.2	RCS function and validation through analytic approximation	19
3.3	Radar Cross Section (RCS) of space debris modeled as spheres of different	
	radii	19
3.4	Received power variation as a function of frequency band for debris sizes 1	
	cm & 1 mm	21
3.5	Rectangular Pulse	24
3.6	First 50 samples of the Gold Sequence	25
3.7	Original Pulse vs Modulated Pulse	25
3.8	Phase difference Original Pulse vs Modulated Pulse	25
3.9	Normalized Autocorrelation function for MonoPulse and Modulated Pulse	26
3.10	Comparison between Monostatic setups: (a) Satellite and (b) Ground Radar	27
3.11	1 ()	
	Received Power for $f_c = 20 \text{ GHz} \dots \dots \dots \dots \dots \dots$	29
	Received Power for $f_c = 12 \text{ GHz} \dots \dots \dots \dots \dots$	30
	Range Resolution vs Maximum detectable Range Comparison	30
	P_R vs altitude - METOP SG Monostatic	32
	Range Resolution vs Maximum Detectable Range- METOP SG Monostatic	33
	P_R vs altitude - HY2 Monostatic	34
	Range Resolution vs Detection Range Limit - HY2 Monostatic	35
	Received Power vs altitude-TIRA	36
	Range Resolution vs Detection Range Limit - TIRA	37
	Received Power vs Altitude-HUSIR	38
	Range Resolution vs Detection Range Limit - HUSIR	39
3 23	Received Power against distance for monostatic and histatic setup	40

3.24	Bistatic scenario	41					
3.25	Distance Tx-debris, and results for Distance Rx-debris for norm and function	43					
3.26	Tx-debris distance from norm and compute distance function						
3.27	Received power vs altitude for two carrier frequencies						
3.28	Comparison of range resolution vs maximum detectable range at different						
	carrier frequencies	46					
3.29	Received Power vs Altitude - Tx: $METOP - SG$ / Rx: $IRIS^2$ -like low orbit	46					
3.30	Range Resolution vs Detection Range Limit	47					
3.31	Received Power vs Altitude - Tx: $HY2$ / Rx: $IRIS^2$ -like low orbit	48					
3.32	Range Resolution vs Detection Range Limit	49					
3.33	Received Power vs Altitude - Tx: TIRA / Rx: $IRIS^2$ -like high orbit	50					
3.34	Range Resolution vs Detection Range Limit	50					
3.35	Received Power vs Altitude - Tx: $HUSIR / Rx$: $IRIS^2$ -like high orbit	51					
3.36	Range Resolution vs Maximum Detectable Range	52					
3.37	MDR vs Altitude - 1 cm	53					
3.38	MDR vs Altitude - 1 mm	53					
3.39	MDR vs Altitude, only the valuable results kept - 1 cm debris	54					
	MDR vs Altitude, only the valuable results kept - 1 mm debris	55					
3.41	RCS optimal frequency band	56					
3.42	Range Resolution vs MDR, HUSIR @ 10 GHz(RED) / HUSIR @ 20 GHz						
	(Brown)	57					

Chapter 1

Introduction

Satellite operators, insurance and the long-term viability of orbital activities are all at risk due to the constantly increasing amount of space debris. The HDI Global Specialty Study of 2023 [1] examines the important events that have led to the accumulation of debris, its dynamic environment, and its technical classification. The mitigation and repair techniques to enhance space debris detection and trackability are the main emphasis of this thesis.

Orbital congestion has dramatically increased as a result of the quick expansion of the commercialization and strategic use of space. The buildup of space trash, or man-made, non-functional objects orbiting the Earth, is a major effect of this expansion. The number of such objects has increased to critical levels since 2000, making more dangerous both current and upcoming operations that can lead to possible collision and damage as shown in fig. 1.1

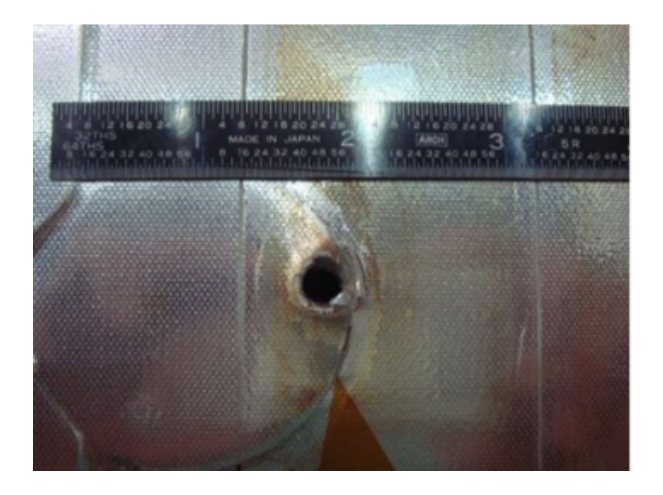


Figure 1.1: Damage caused by space debris [1]

The study by HDI Global Specialty [1] SE aims is to provide a comprehensive overview of the space debris landscape from both technical and risk-management standpoints, the report emphasizes how the growing threat affects not just satellite design and operation, but also underwriting and liability frameworks. Space debris includes everything from defunct satellites and abandoned rocket stages to minuscule paint flecks and tools lost during spacewalks. The key concerns surrounding debris are:

• Collision Risk: Traveling at speeds up to 10 km/s, even a 1 cm object can cause catastrophic damage to spacecraft.

- Service Loss: A collision can render communication, navigation, or Earth observation services inoperable.
- Chain Reactions: Collisions generate more debris, escalating the risk of further collisions a concept known as the Kessler Syndrome.

Data-driven projections indicate a rising trend in both collision probability and debris concentration, particularly in Low Earth Orbit (LEO).

The source of these debris can be associated to different factors but mainly we can distinguish two subclasses:

- Deliberate sources: separation mechanisms (e.g., spring-loaded bolts), structural deployment leftovers (e.g., solar panel holders), anti-satellite weapon tests (e.g., China's 2007 ASAT test), upper stage rocket bodies, defunct satellites left in uncontrolled orbits.
- Accidental Sources: unintended explosions (e.g., battery or tank ruptures), satellite collisions (e.g., Iridium 33 and Cosmos 2251), human error (e.g., tools lost during EVAs).

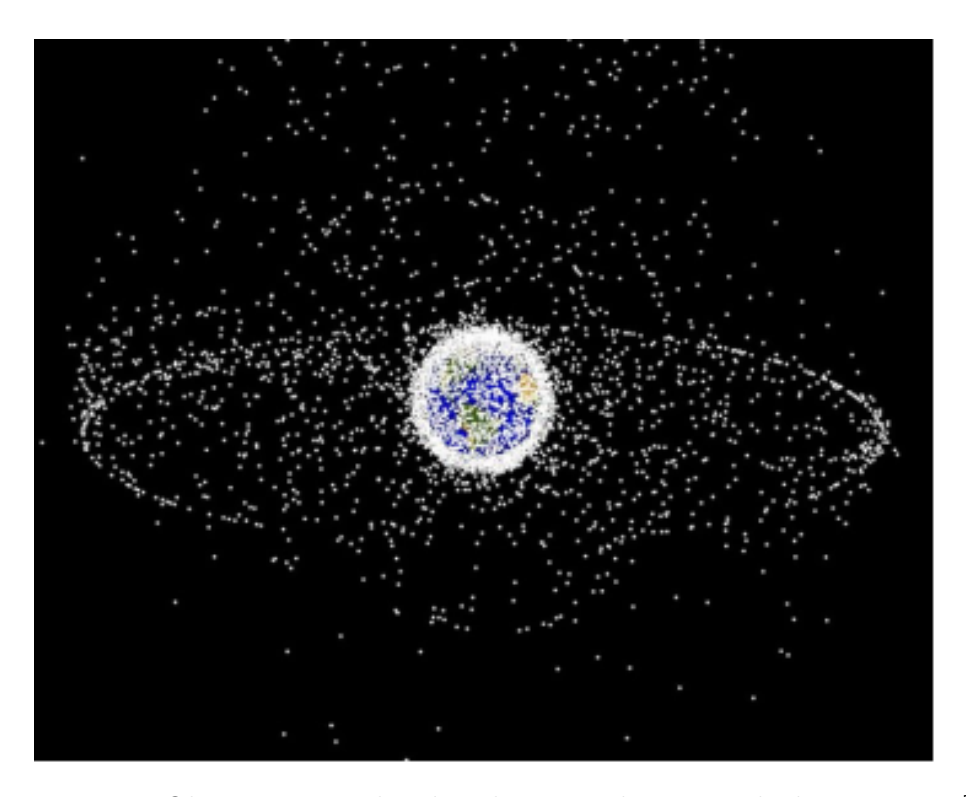


Figure 1.2: Objects in Earth orbit that were being tracked as in 2019 [1]

1.1 Space debris classification and Distribution

As stated in [1] the most important and obvious metrics to use in order to classify the space debris are the size and altitude. Physical size is import, not only to state the risk that the debris can produce but also to confirm the reliability of tracking of these debris, even because, as defined in [2], the debris can be cataloged when it is tracked reliably

enough so that a precise orbit can be determined and updated over time. In[3] the ESA categorizes the space debris by size in three main classes and defines the tracking and number of those in orbit.

Category	Diameter	Number in orbit	Trackability
Large	> 10 cm	36,500	Tracked and catalogued
Medium	1 cm to 10 cm	1,000,000	Trackable but with lower reliability
Small	1 mm to 1 cm	130,000,000	Not currently tracked

Table 1.1: ESA categorisation of space debris by size, approximate numbers in orbit as of August 2022, and trackability

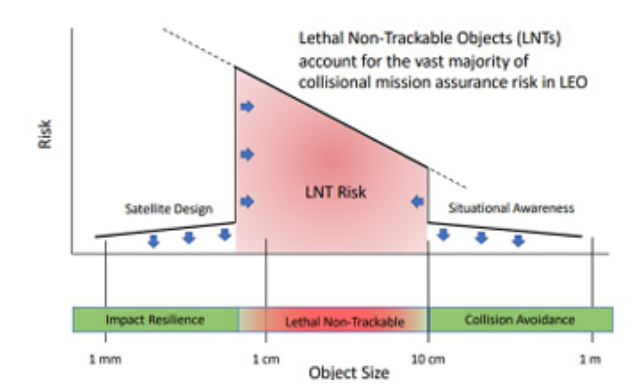


Figure 1.3: Impact of LNT on the risk profile for a typical LEO satellite [4], 2019

The vast majority of space debris—over 99%—consists of small-sized objects that are not currently tracked. This lack of trackability severely limits the ability to predict and avoid potential collisions. As stated before a particularly concerning subset of this debris is known as Lethal Non-Trackable (LNT) objects, typically ranging from 1 mm to 1 cm in diameter. Though too small to be tracked, LNT debris is large enough to cause catastrophic damage to operational satellites. These objects represent more than 99% of the mission-terminating collision risk for typical Low Earth Orbit (LEO) satellites. LNT debris primarily originates from satellite explosions, rocket body breakups, and past major collisions. Several satellite anomalies and failures, such as WorldView-2, Sentinel-1A, AMC-9, and Express 80, are suspected to have been caused by such non-trackable debris. The altitude is another important parameter for space debris since based on the orbit the speed and the number of satellites is different, between the three existing region (LEO, MEO. GEO) Low Earth Orbit (LEO) is widely recognized as the orbital region with the highest probability of collisions. A 2017 study by Frey and Lemmens estimated a cumulative collision probability of 1.5×10^{-1} per year in LEO—equivalent to one collision every seven years. Notably, this estimate excluded objects smaller than 10 cm. Despite this limitation, there is a general consensus within the space industry that the likelihood of collision in LEO is two to three orders of magnitude higher than in other orbital regions. Several factors contribute to the elevated collision risk in LEO:

- High density of both active satellites and debris,
- Greater orbital velocities,
- Presence of clusters of massive, non-operational derelict objects.

According to data from the U.S. Space Surveillance Network (SSN), the spatial distribution of tracked objects varies with altitude. Above 650 km, the probability of debris-on-debris collisions surpasses that of debris colliding with operational spacecraft.

Some satellites in LEO, particularly those equipped with propulsion systems, can perform end-of-life (EOL) deorbit manoeuvres, enabling atmospheric re-entry and disintegration. However, many spacecraft lack this capability or do not perform such maneuvers. Instead, they rely on atmospheric drag to gradually reduce altitude—a process that can take months to decades depending on the orbital parameters. In the highest altitudes of LEO, natural deorbiting is often insufficient, leaving these objects in orbit indefinitely and contributing to long-term collision risk.

Collisions in LEO are significantly more destructive than those in Geostationary Orbit (GEO), primarily due to higher relative velocities and greater orbital inclinations (28°–115° in LEO versus 0°–15° in GEO). On average, collisions in LEO are approximately 400 times more destructive than those in GEO. Of particular concern are the massive derelict objects concentrated in certain LEO clusters. A single collision involving such objects could generate tens of thousands of Lethal Non-Trackable (LNT) debris fragments, posing a persistent and severe hazard to the orbital environment.

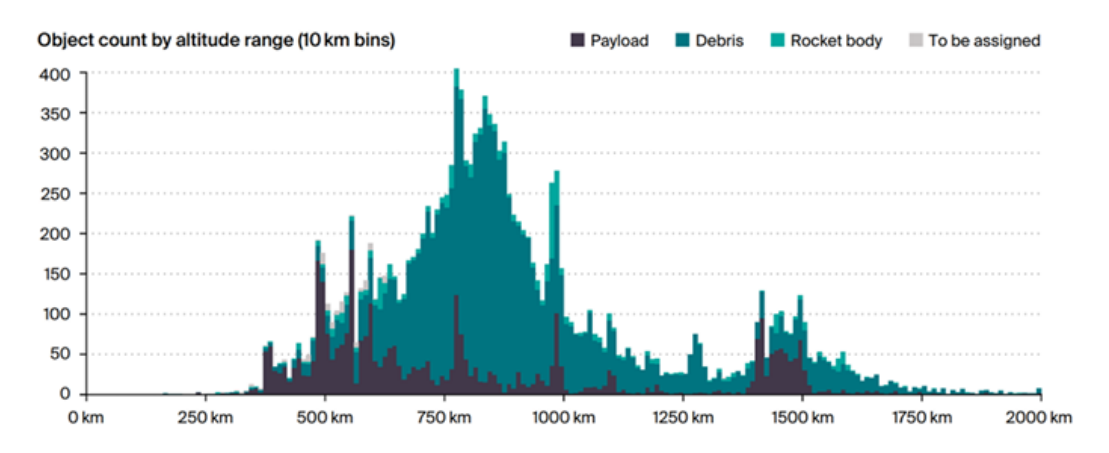


Figure 1.4: Catalogue of LEO space objects tracked by the US SSN as of May 2020. Note that the 'Payload' category comprises both operational and non-operational objects [1]

1.2 Detectability and Trackability Criteria for Space Debris

The ability to detect and track space debris using ground-based radar systems is determined by a set of physical and technical parameters, which govern whether an object can be observed, cataloged, and monitored over time. These criteria are not governed by a single international standard, but rather by shared practices, technical constraints, and recommendations by major space agencies and organizations such as ESA, NASA, and ITU.

A key factor in the detectability of space debris is the minimum detectable object size, which varies depending on orbital altitude and sensor technology. In Low Earth Orbit (LEO), radar systems can typically detect objects as small as 5–10 cm in diameter, while in Medium and Geostationary Earth Orbits (MEO and GEO), only objects larger than 30 cm to 1 meter are detectable [5]. This capability is enabled by high-gain antennas such as large parabolic reflectors or phased arrays, which concentrate energy and maximize the signal-to-noise ratio (SNR) for distant targets [6].

Another essential parameter is the Radar Cross Section (RCS), a measure of how detectable an object is to radar based on its size, shape, and material. An RCS above 0.01–0.1 m² is typically required for reliable detection in LEO [7]. Additionally, the radar system configuration—monostatic, bistatic, or multistatic—along with operational parameters such as transmitted power, frequency, and range resolution, directly influences the minimum detectable size and tracking accuracy. For instance, systems operating in the L- or X-band with transmission powers exceeding 10 kW and antenna gains above 30 dBi are capable of tracking fast-moving LEO debris with positional accuracies of under 100 meters [6][8].

For an object to be trackable, it must be observed over multiple passes to determine its orbital elements accurately. This typically involves estimation of the six classical orbital parameters (e.g., semi-major axis, inclination, eccentricity) with sufficient precision to enable future position prediction and collision risk assessment. Accurate tracking requires both angular and Doppler resolution, often achievable through phased-array radars or radar interferometry techniques [6].

The catalogability of a space debris object implies not only detectability and orbital estimation but also the capability to consistently identify and correlate successive observations. This is the operational goal of networks such as the U.S. Space Surveillance Network (SSN), which maintains the largest public catalog of space objects through continuous radar and optical tracking [8].

In summary, ground-based radar systems enable effective debris detection and tracking provided that debris size, RCS, orbit, and sensor configuration align with the system's sensitivity thresholds. These parameters form the operational backbone of space situational awareness (SSA) and are critical to global efforts in space traffic management and collision avoidance.

1.3 Detection from ground

Ground-based sensors, particularly radars, play a critical role in debris monitoring. Radar systems, along with optical telescopes and laser tracking technologies, are used to detect, track, and catalogue objects with a characteristic size exceeding 5–10 cm in LEO, and greater than 0.3–1.0 meters in Medium Earth Orbit (MEO) and Geostationary Earth Orbit (GEO) [5].

The United States operates the most comprehensive surveillance network through its Space Surveillance Network (SSN), managed by the United States Strategic Command (USSTRATCOM). The network includes both radar and optical sensors, contributing to the world's most extensive catalogue of orbital debris. The Combined Space Operations Center (CSpOC) processes observational data and provides orbital parameters via Two-Line Element (TLE) sets. Inspired by the U.S. system, similar surveillance initiatives have been established by Roscosmos (Russia), JAXA (Japan), and ESA (Europe), among others. While data from these programs are often shared for international cooperation, the availability of open-access literature reporting quantitative results from debris tracking campaigns remains limited.

Focusing on radar-based systems, typical configurations include monostatic, bistatic, and multistatic systems. Monostatic radars use a single platform for both transmission and reception, whereas bistatic and multistatic systems employ separate antennas at distinct locations, allowing for improved spatial coverage [5].

From a signal perspective, radar transmissions are categorized as either continuous wave (CW) or pulsed. CW radars are ideal for measuring Doppler shifts and velocity, while pulsed radars provide range information critical to determining the object's position.

The most widely used radar architectures for space debris include:

- Parabolic reflectors, which offer high gain and accurate mechanical tracking, making them suitable for precise orbit determination;
- Phased arrays, which electronically steer beams to scan large sky areas rapidly and are effective for detecting uncatalogued debris;
- Radar interferometers, which leverage multiple antennas spaced over long baselines to estimate object positions via phase differences.

These systems, often integrated into national or international sensor networks, form the backbone of current efforts in global space surveillance.

Chapter 2

State of the Art in space detection

2.1 Debris Sensing Based on LEO Constellations: An Intersatellite Channel Parameter Estimation Approach

2.1.1 Introduction

The work by Liu et al. [9] proposes a paradigm shift in debris sensing, leveraging the intersatellite links (ISLs) inherent in dense LEO constellations (e.g., Starlink, OneWeb) as opportunistic bistatic radar networks. This approach transforms existing communication infrastructures into sensing platforms without requiring dedicated debris detection payloads, potentially reducing costs and facilitating scalable debris monitoring.

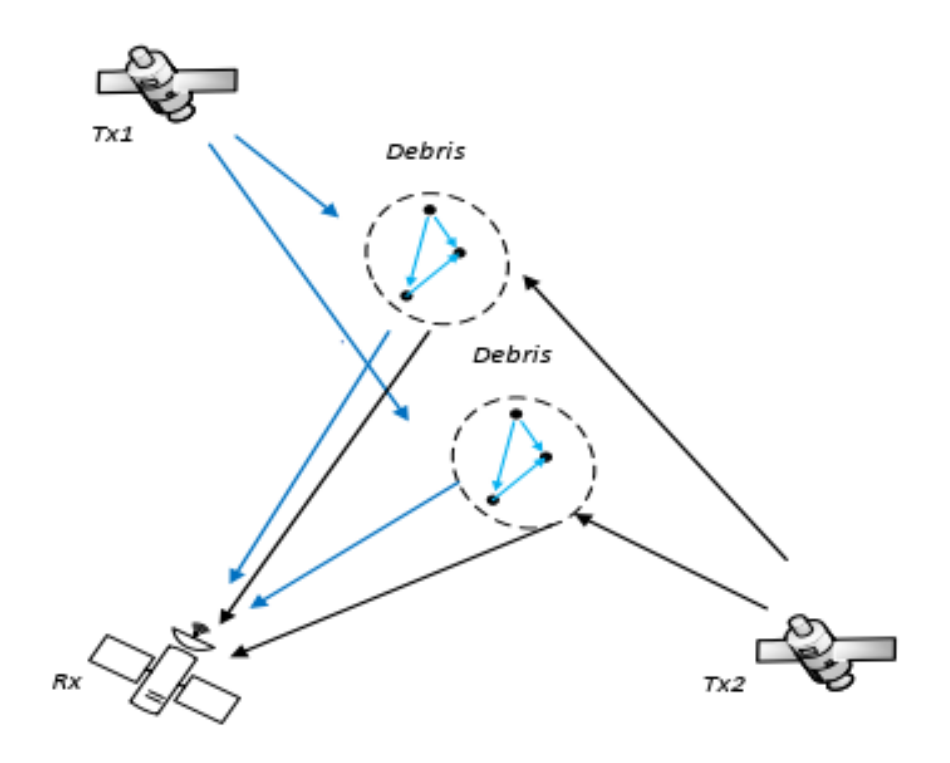


Figure 2.1: Scenario kind for sensing based on LEO

2.1.2 Conceptual Framework and Motivation

Traditional debris monitoring typically relies on monostatic ground-based radars or optical telescopes. While effective for larger objects, their detection performance deteriorates significantly for sub-10 cm debris. Moreover, the coverage provided by these assets is limited by orbital geometry, weather conditions, and the need for costly dedicated observation campaigns.

Liu et al. propose a two-stage detection concept:

- 1. **Opportunistic sensing**: Utilize intersatellite communication signals to detect and estimate coarse debris parameters.
- 2. **Targeted refinement**: For debris deemed threatening, dedicated follow-up observations can refine localization and trajectory estimates.

This two-step process reduces the burden on dedicated sensors while maintaining sufficient detection capabilities to flag potential hazards.

In the opportunistic sensing phase, each ISL forms a bistatic radar configuration. The transmitted signal reflects off debris objects and is subsequently captured by a receiving satellite. The non-line-of-sight (NLoS) propagation paths induced by debris reflections encode valuable information about their location and motion.

2.1.3 Signal and Channel Modeling

The study formulates a stochastic geometric model of the intersatellite debris sensing channel. Key modeling assumptions include:

- Debris objects are densely distributed and *clustered* in space.
- Each cluster consists of multiple scatterers whose individual reflections are similar but not fully resolvable.
- The multipath components can be modeled as amplitude- and phase-perturbed versions of a cluster "centroid" path.

Mathematically, the channel impulse response (CIR) of each cluster is expressed as:

$$h_{l,k}(t) = h_{lc}(t) \left(1 + \Delta \alpha_{lk} \right) e^{j\Delta \phi_{lk}}, \tag{2.1}$$

where:

- $h_{lc}(t)$ denotes the centroid (dominant) path,
- $\Delta \alpha_{lk}$ and $\Delta \phi_{lk}$ are zero-mean Gaussian variables modeling random amplitude and phase deviations within the cluster.

The model also accounts for *range-Doppler coupling*, an important phenomenon in fast-moving LEO environments where the relative velocities of satellites and debris introduce non-negligible frequency shifts and distortions in delay estimation.

2.1.4 Channel Parameter Estimation: SAGE and SAGE2 Algorithms

Estimating the parameters of the reflected signals—particularly delays and amplitudes—is essential for localizing debris clusters. Traditional estimation approaches such as *Expectation*+ *Maximization* (EM) and its accelerated form, the *Space-Alternating Generalized EM* (SAGE) algorithm, are widely used in high-resolution multipath channel estimation.

However, conventional SAGE assumes that multipath components are resolvable and can be sequentially estimated as independent contributions. In dense debris clusters, this assumption does not hold, resulting in model mismatch and computational inefficiency.

To overcome this, Liu et al. propose an improved method called the *nested expectation-based SAGE* (SAGE2), which:

- Estimates parameters at the *cluster level* instead of the individual paths.
- Reduces the number of parameters to estimate.
- Improves convergence speed in the presence of dense, correlated multipaths.

In SAGE2, the algorithm iteratively refines estimates of:

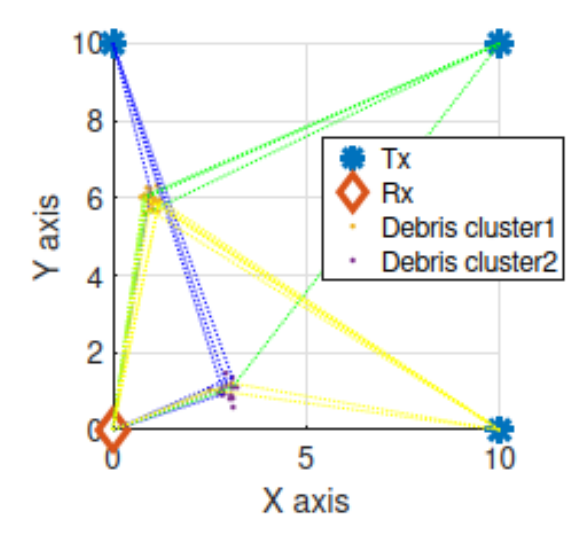
- 1. Cluster centroid delays τ_{lc} ,
- 2. Cluster amplitudes α_{lc} ,
- 3. The effective number of paths l_K within each cluster.

This formulation significantly reduces estimation complexity and accelerates convergence compared to conventional SAGE.

2.1.5 Simulation Setup and Results

The authors validate their approach through extensive simulations:

- Scenario: Three transmitter satellites and one receiver satellite observe a $1,000 \times 1,000$ km area containing two debris clusters.
- **Key parameters:** 14 GHz carrier frequency, 1 MHz sampling rate, high SNR (40 dB), realistic satellite and debris velocities.
- Metric: Convergence speed and localization accuracy.



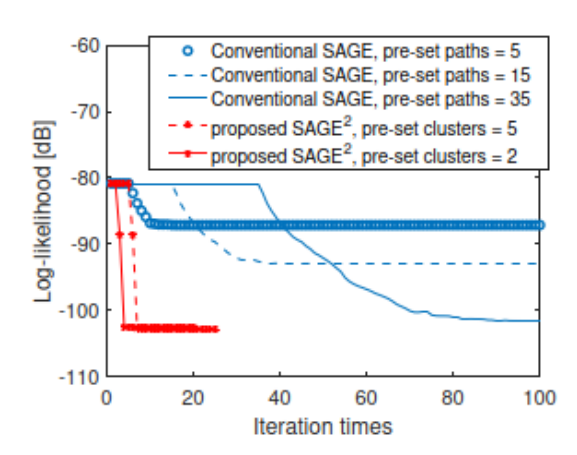


Figure 2.2: Opportunistic MP between TXs and RXs, where the blue, green, and yellow dashed lines are TX1-RX, TX2-RX, TX2-RX.

Figure 2.3: Comparison with conventional SAGE: iteration time.

The simulation demonstrates that:

- Conventional SAGE requires prior knowledge of the exact number of paths (which is difficult to obtain) and converges slowly.
- SAGE2 requires only an approximate number of clusters (more easily estimated) and achieves faster convergence.
- The cluster centroids estimated by SAGE2 can be directly used for coarse debris localization via time-difference-of-arrival (TDoA).

Notably, the results show that SAGE2 achieves optimal likelihood convergence in fewer iterations compared to SAGE, highlighting its computational advantage. This work provides several important contributions to the field of space situational awareness:

- 1. **Integration of sensing and communication**: A feasible approach to leverage ISLs in commercial satellite constellations for debris detection without additional hardware.
- 2. Cluster-based channel modeling: A more realistic representation of dense debris fields compared to sparse multipath models.
- 3. **Algorithmic innovation**: SAGE2 extends classical estimation frameworks to better handle unresolvable multipath scenarios.
- 4. **Operational relevance**: The method can serve as a first-layer detection mechanism to flag potentially threatening debris for further refinement.

The approach proposed by Liu *et al.* aligns well with emerging trends in *integrated sensing* and communication (ISAC). As satellite constellations continue to expand, the opportunistic use of communication signals for environmental monitoring offers a compelling path toward scalable, cost-effective debris surveillance.

Future research directions could include:

- Addressing range-Doppler coupling effects through advanced waveform design or multi-frame processing.
- Extending the model to account for inter-cluster scattering.
- Incorporating real ISL data to validate performance in operational scenarios.

2.2 Affordable Processing for Long Coherent Integration of Weak Debris-Scattered GNSS Signals with Inconsistent Doppler

2.2.1 Introduction

Mahmud et al. [mahmud2016affordable] address the problem of detecting extremely weak signals resulting from Global Navigation Satellite System (GNSS) transmissions scattered off space debris in Low Earth Orbit (LEO). Unlike conventional direct GNSS reception, these signals arrive with significantly reduced power and exhibit complex, time-varying Doppler shifts that challenge standard processing techniques.

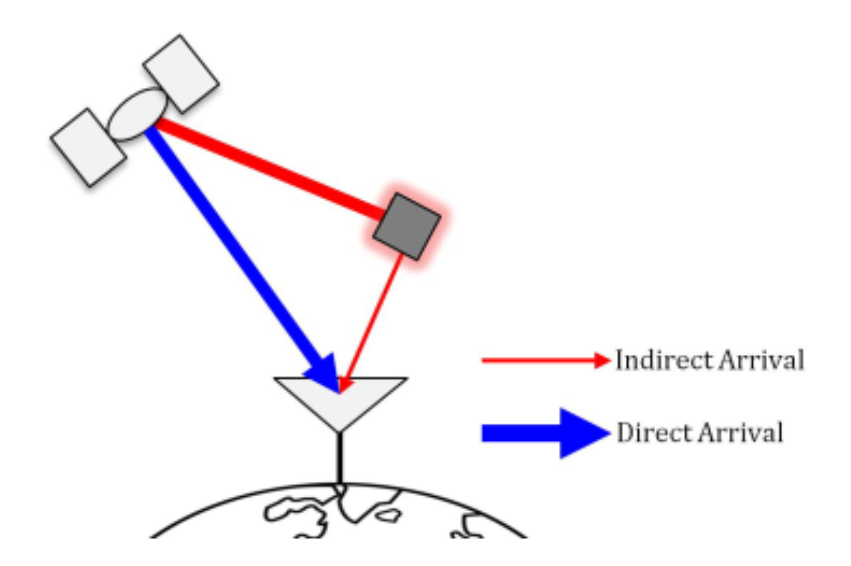


Figure 2.4: Direct and Scattered GNSS signal

Detecting debris-scattered GNSS signals is inherently challenging for several reasons:

- The received power of the scattered signal is orders of magnitude lower than that of the direct GNSS signal.
- To accumulate sufficient signal energy, very long coherent integration periods (on the order of hundreds of seconds) are required.
- Inconsistent and time-varying Doppler shifts, due to the relative motion of the GNSS satellites, debris, and receiver, introduce phase errors that degrade coherent integration gain.
- Processing such long-duration correlations at high sampling rates demands substantial computational resources.

Traditional acquisition methods, such as those using the Fast Fourier Transform (FFT) or non-coherent integration, either do not achieve the required processing gain or are computationally prohibitive.

2.2.2 Proposed Processing Approach

To overcome these challenges, the authors propose a novel multi-stage processing strategy inspired by super-heterodyne receivers. The method comprises the following key steps:

- 1. Correlation and Integrate & Dump (I&D): The incoming signal is first correlated with a replica signal containing the expected PRN code, data modulation, and Doppler frequency. This matched filtering operation isolates the target signal components.
- 2. The result is passed through an I&D operation, which effectively acts as a low-pass filter and decimator. This reduces the bandwidth of the signal to audio frequencies (AF), greatly decreasing the data rate while preserving the uncertainty volume necessary for tracking.
- 3. Post-correlation Phase Correction: In the final step, long-duration coherent integration is achieved by summing the decimated audio-frequency samples while applying appropriate phase adjustments to account for the residual phase evolution. These corrections may involve non-linear phase models to capture the Doppler variations over time.

This approach enables the efficient construction of trajectory hypotheses over long observation windows without re-processing the entire high-rate signal for each candidate hypothesis.

2.2.3 Computational Considerations

To illustrate the computational burden, consider the following estimation:

Assuming a Nyquist sampling rate f_s of 2 MHz and an integration time T=600 seconds, the number of multiply-accumulate operations (MACs) required to process each trajectory hypothesis directly at RF is:

$$N = f_s \times T = (2 \times 10^6) \times 600 = 1.2 \times 10^9 \text{ MACs.}$$

In contrast, after the initial I&D step decimates the signal to an audio rate f_a (e.g., 10 kHz), the same operation requires only:

$$N_{\rm AF} = f_a \times T = (10^4) \times 600 = 6 \times 10^6 \text{ MACs.}$$

This represents a computational saving of approximately 200-fold.

Moreover, since trajectory hypotheses in orbital tracking are sparse and governed by momentum conservation constraints, many candidate trajectories share similar phase evolution, enabling further processing efficiencies through intermediate coherent integrations.

2.2.4 Experimental Validation

The authors validate their approach using real GNSS data collected from a GPS Block IIF satellite. The signal was recorded at an intermediate frequency of 32.42 MHz and sampled at 128 Msps.

Several scenarios were considered to demonstrate:

- The capability of the technique to handle deliberate Doppler misestimation.
- The effectiveness of post-correlation phase corrections to re-align the signal coherently across the observation interval.
- The resilience to data bit errors in the replica signal.

For instance, Figure 7 in the article illustrates how non-linear phase drift, resulting from unmodeled Doppler variations, accumulates over time. Subsequent phase rotation in the audio-frequency domain successfully removes this error, yielding coherent integration over the full duration. This work offers several important contributions:

- 1. **Feasible Long-duration Integration:** A practical method for achieving long coherent integration of weak signals scattered by debris, without prohibitive computational costs.
- 2. Robustness to Inconsistent Doppler: The approach tolerates non-linear and unpredictable phase variations, a significant advantage over conventional FFT-based methods.
- 3. **Broad Applicability:** Although demonstrated with GNSS signals, the technique can be adapted to any passive radar illumination source.

In the context of space situational awareness, this method could enable the detection and tracking of small debris using cost-effective receivers and commercially available signals of opportunity, thereby reducing the barriers to more comprehensive debris monitoring. The processing strategy proposed by Mahmud *et al.* represents an important step toward affordable, high-sensitivity passive radar detection of space debris. By decoupling the computationally intensive correlation step from the flexible hypothesis testing step, the method achieves substantial gains in efficiency without sacrificing detection

2.3 Detection of Small-Sized Space Debris Using Laser Communication Systems

In recent years, the development of high-data-rate laser communication systems has opened new opportunities not only for data transfer but also for active debris detection. An example of such an integrated approach is the Laser Communications Demonstration Equipment (LCDE) installed onboard the Japanese Experimental Module (JEM) attached to the International Space Station (ISS). As described by Arimoto et al. [10], the LCDE was originally designed to demonstrate optical communication at bit rates exceeding 2.5 Gbps. However, the system also incorporates capabilities for acquisition and tracking of small targets, making it an ideal platform for debris observation experiments.

The basic concept of this approach is to first detect sunlight reflected from the debris surface to estimate its position and angular velocity. Once the target is acquired, the LCDE directs a narrow laser beam towards the debris, and the reflected signal is captured by the onboard receiver. By measuring the turnaround delay and the Doppler shift of the reflected signal, it becomes possible to estimate both the distance and relative velocity of the object. Figure ?? illustrates the known distribution of debris at approximately 500 km altitude, highlighting the lack of observational data for objects smaller than 10 cm [10].

One of the critical aspects of the LCDE experiment concerns the optimization of the transmitted beam divergence. The system employs a Cassegrain antenna configuration,

and the emitted Gaussian beam is both truncated by the primary mirror and obscured by the secondary mirror. Arimoto et al. [10] demonstrate that these factors lead to significant power loss, especially when targeting debris at relatively short distances (e.g., 2 km). Numerical Fresnel integration was used to model near-field beam profiles, revealing that convergent beam settings can substantially improve antenna gain for debris detection. However, the system must maintain acceptable performance for the primary long-range communication experiment as well, requiring a trade-off in beam divergence selection.

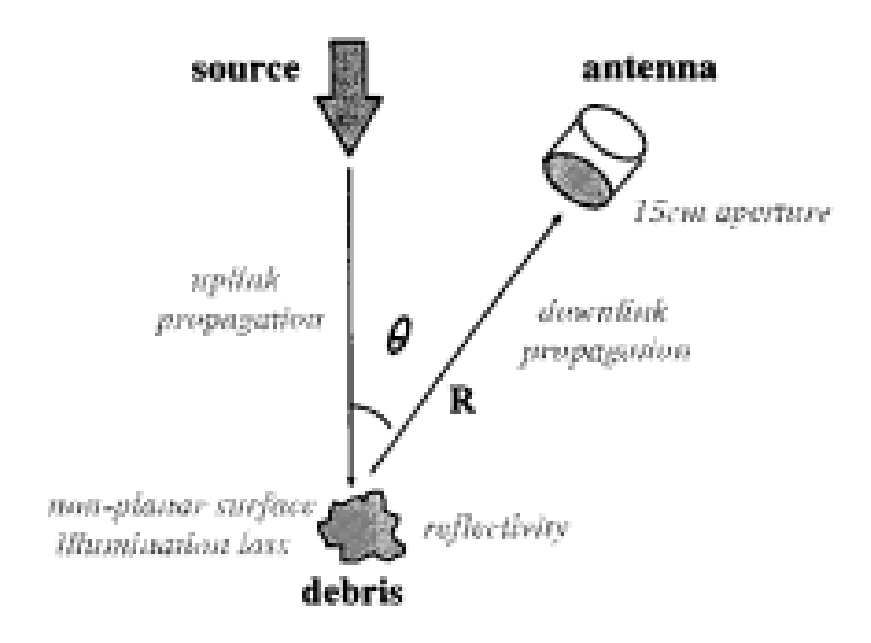


Figure 2.5: Link Scheme

The link budget analysis indicates that only about 4.78% of the initial transmitted power effectively illuminates a 1 cm diameter debris target at a distance of 2 km [10]. Considering the Lambertian reflection model and the associated propagation losses, the resulting received signal power is extremely low. This imposes stringent requirements on the sensitivity and noise performance of the detection system.

Three detection architectures were evaluated: direct detection using an InGaAs avalanche photodiode (APD), an Er-doped fiber amplifier (EDFA) front-end system, and a coherent homodyne detection approach. The APD-based system demonstrated poor sensitivity due to high amplifier noise, while the homodyne system offered excellent signal-to-noise ratio (SNR) in principle. However, the homodyne method was deemed impractical because of the large Doppler shifts (up to 20 GHz) induced by debris motion relative to the ISS. Consequently, the EDFA front-end was selected as the most promising candidate, with post-detection correlation processing anticipated to improve SNR by more than 30 dB [10].

These results emphasize that laser communication payloads can play a dual role, significantly enhancing situational awareness of the orbital environment. By incorporating additional processing capabilities and optimizing optical parameters, future missions may be able to characterize populations of small debris objects in near real-time. Such capabilities are critical not only for protecting the ISS and other spacecraft from impact but also for informing debris mitigation and remediation strategies in the coming decades.

Chapter 3

Space Debris Detection with $IRIS^2$ -like Constellation

In this section, we aim to conduct a comprehensive analysis of the potential resources and technologies that could be integrated with the newly proposed IRIS satellite constellation for the purpose of detecting and tracking (LNT) space debris. The analysis encompasses both space-based assets and ground-based detection systems, with the objective of evaluating their respective capabilities, limitations, and synergies. Furthermore, the proposed solutions will be systematically compared against current state-of-the-art debris detection methods to assess their relative effectiveness, feasibility, and potential for operational integration. Through this comparative study, we seek to determine whether the adoption of the $IRIS^2$ -like constellation for debris monitoring represents a technically and economically viable advancement over existing methodologies. The considered constellation and ground radar are the following:

- $IRIS^2$ -like : 1200 km 700 km
- METOP sg: 832 km
- HY 2:932 km
- Skymed*: 619 km (Removed due to the low altitude)
- HUSIR: On earth
- TIRA: On earth

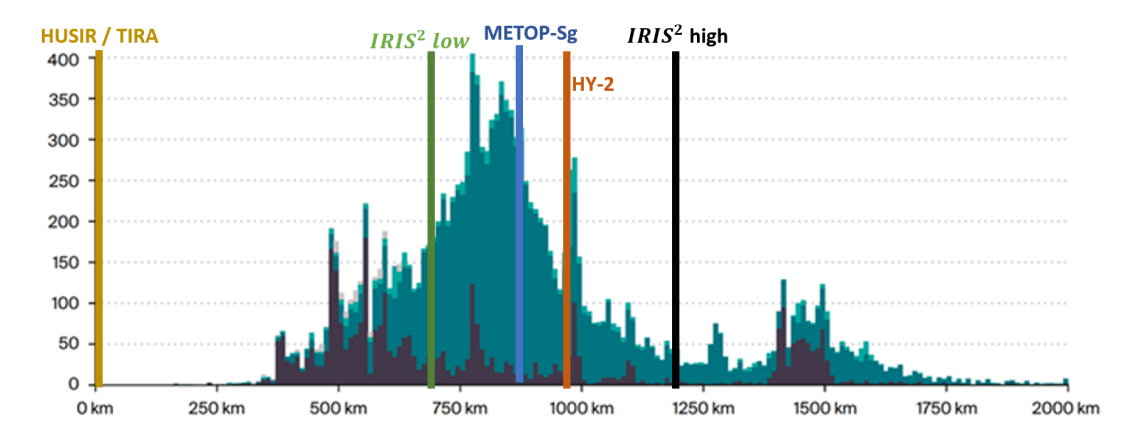


Figure 3.1: Constellation and Ground RADAR considered for the analysis

The analysis will be divided considering monostatic and bistatic setups, and all the possible combination are shown in the following table:

$\mathbf{TX}\downarrow\mathbf{RX}\rightarrow$	TIRA (GS, L-band 1 GHz, Gr = 52.34 dBi)	HUSIR (GS, X-band 10 GHz)	IRIS2 (Altitude: 700 km, Ka-band, $Gr = 10 dBi$)	MetOp SG (Alt: 830 km, C-band 5.33 GHz)	HY-2 (Altitude: 932 km, Ku-band)	IRIS2 (Altitude: 1200 km , Ka-band, $\text{Gr} = 10 \text{ dBi}$)
TIRA (GS, L-band, EIRP: 112.34 dBw)	X					X
$\begin{array}{ll} \mathrm{HUSIR} \ (\mathrm{GS}, \ \mathrm{X\text{-}band}, \ \mathrm{EIRP:} \ 126.38 \\ \mathrm{dBw)} \end{array}$		X				X
IRIS2 (Altitude: 700 km, Ka-band, EIRP: 57.96 dBw)			LOW ALTITUDE			
$\begin{array}{lll} \rm MetOp \ SG \ (Alt: \ 830 \ km, \ C\mbox{-}band, \\ \rm EIRP: 93.55 \ dBw) \end{array}$			X	X		
HY-2 (Altitude: 932 km, Ku-band, EIRP: 67.32 dBw)			X		X	
IRIS2 (Altitude: 1200 km, Ka-band, EIRP: 57.96 dBw)			X			X

Table 3.1: Configuration matrix: transmitter (TX) and receiver (RX) combinations among ground and space systems.

3.1 RCS

Since the primary objective of this analysis is to assess the effectiveness and capabilities of various sensing assets under different operational scenarios, a simplification has been adopted to facilitate the evaluation. Specifically, space debris are idealized as spherical bodies, enabling the direct application of well-established Radar Cross Section (RCS) formulas for analytical tractability.

Within this framework, an RCS analysis has been carried out for two distinct debris sizes—namely, 1 cm and 1 mm in diameter—to evaluate how each object interacts with electromagnetic waves across a range of frequencies. The aim is to identify the corresponding operating region on the RCS-versus-frequency characteristic curve for each debris dimension. Such an analysis is critical in determining the effective central frequency for the radar setup under consideration.

The central frequency is pivotal in the application of the radar equation, as it significantly influences key performance metrics such as detection range and sensitivity. Consequently, the frequencies selected for this study align with those typically employed by the satellites under investigation, and their central operating points have been carefully delineated and analyzed within this context.

• Ka-Band : 20 [GHz]

• Ku-Band: 13.256 [GHz]

• X-Band : 10 [GHz]

• C-Band : 5.33 [GHz]

• L-band: 1.33 [GHz]

Because the Radar Cross Section (RCS) depends on several variables, the function that best approximates the RCS behavior of a sphere is the Hankel function of the first kind. For a brief review: in the case of electromagnetic scattering from a perfectly conducting sphere, the inherent symmetry ensures that the backscattered waves remain co-polarized with the incident waves, making the cross-polarized component practically negligible. For instance, if the incident wave is Left Circularly Polarized (LCP), the backscattered wave will also be LCP; however, due to the reversal in propagation direction, the receiving antenna detects it as Right Circularly Polarized (RCP). As a result, the co-polarized (PP) backscatter dominates, while the cross-polarized (OP) backscatter can be disregarded.

The normalized backscattered RCS of a perfectly conducting sphere is formally described by a Mie series expansion, which involves both spherical Bessel and Hankel functions.

$$\frac{\sigma}{\pi r^2} = \left(\frac{1}{kr}\right)^2 \sum_{n=1}^{\infty} (-1)^n (2n+1) \left[\frac{kr J_{n-1}(kr) - n J_n(kr)}{kr H_{n-1}^{(1)}(kr) - n H_n^{(1)}(kr)} - \frac{J_n(kr)}{H_n^{(1)}(kr)} \right], \tag{3.1}$$

 $H_n^{(1)}(kr)$ os the Hankel function of the first kind is described by the following behavior and $Y_n(kr)$ is the Bessel function of the second kind:

$$H_n^{(1)}(kr) = J_n(kr) + jY_n(kr), (3.2)$$

Examination of the RCS as a function of the sphere's circumference, expressed in units of the wavelength, reveals three distinct scattering regimes. In the optical region, corresponding to electrically large spheres, the RCS approaches the physical cross-sectional area of the sphere. In the Rayleigh region, relevant for electrically small spheres, the RCS scales with the fourth power of the sphere's radius relative to the wavelength. Between these two extremes lies the Mie (or resonance) region, where the RCS exhibits significant oscillatory behavior due to the interplay of constructive and destructive interference in the scattered fields. The optical region approximation:

$$\sigma = \pi r^2, \qquad r \gg \lambda$$
 (3.3)

The Rayleigh region approximation

$$\sigma = 9\pi r^2 \left(kr\right)^4, \qquad r \ll \lambda \tag{3.4}$$

where **k** is the **Wavenumber**, $k = \frac{2 \cdot \pi}{\lambda}$

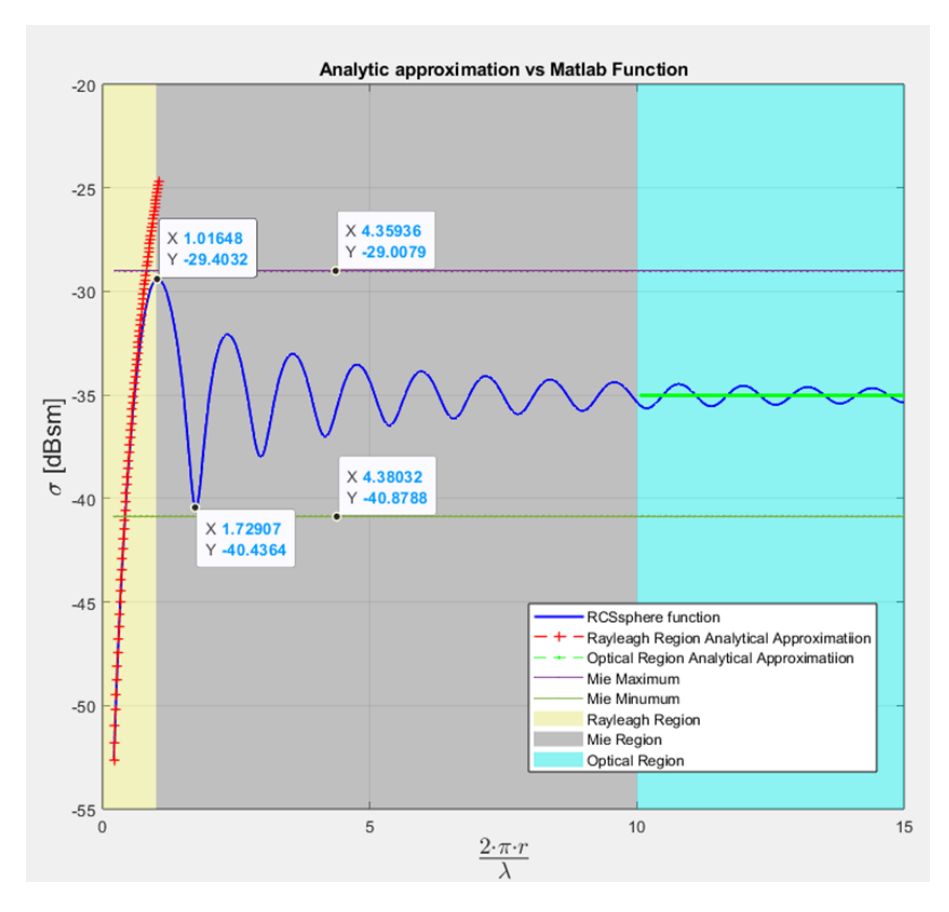


Figure 3.2: RCS function and validation through analytic approximation

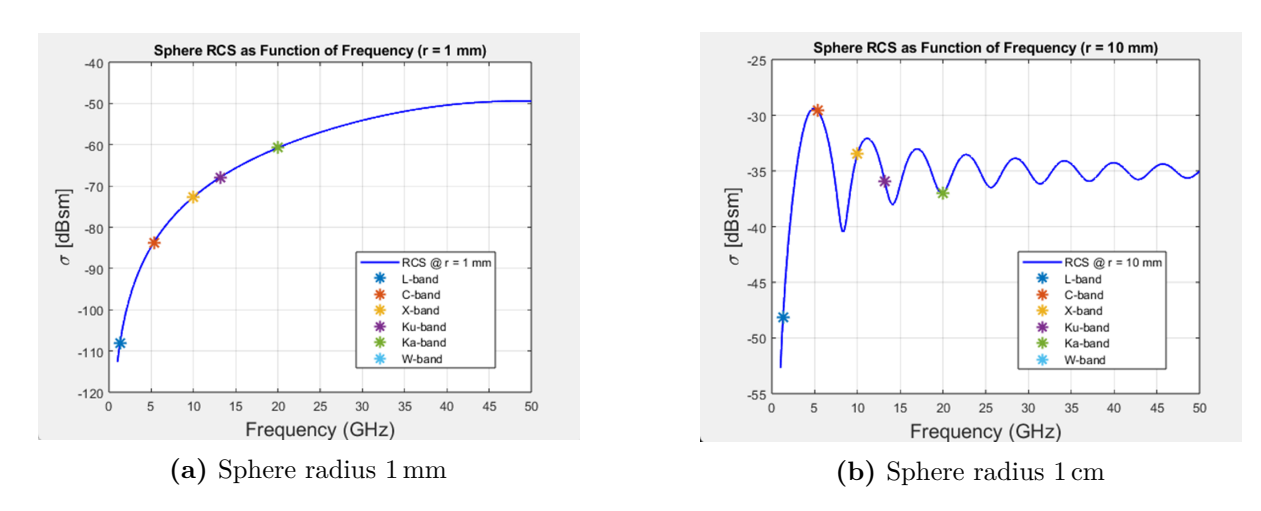


Figure 3.3: Radar Cross Section (RCS) of space debris modeled as spheres of different radii.

The two figures above, (3.3), illustrate the normalized Radar Cross Section (RCS) as a function of frequency for spherical space debris with radius of 1 cm and 1 mm, respectively. In the case of the 1 cm debris, the RCS exhibits a clear oscillatory behavior across the frequency range, with distinct resonance peaks and nulls. This is characteristic of the Mie scattering regime, where the size of the object is comparable to the wavelength of the incident electromagnetic wave. Resonances begin to appear around 5–6 GHz and persist through higher frequencies, with multiple operational radar bands (C, X, Ku,

and Ka) intersecting regions of varying RCS magnitude. This implies that the detection performance for such debris strongly depends on the specific operating frequency, as the RCS can vary significantly even within the same frequency band.

In contrast, the 1 mm debris falls within the Rayleigh scattering regime, where the object size is much smaller than the wavelength. The corresponding RCS curve is smoother and increases monotonically with frequency, with no apparent resonances. At lower frequencies (e.g., L-band and C-band), the RCS remains extremely low, rendering detection in those bands highly challenging. Only at higher frequencies—particularly above 20 GHz, near the Ka-band—does the RCS reach values that may support feasible detection. This comparative analysis highlights the importance of selecting the appropriate central frequency based on the size of the target debris. To enhance the visualization of how the Radar Cross Section (RCS) influences the received power and detection capabilities, an analysis was conducted using the parameters specified in the following table. This study aims to illustrate the variation in received power across different frequency bands for two distinct debris sizes according to the following set of parameters that corresponds to the $IRIS^2$ setup:

Parameters	Value
Distance	1200 km
Carrier Frequency	[0,300] Ghz
Transmit Power	1 W
Antenna Gain TX	36 dBi
Antenna Gain RX	30 dBi

Table 3.2: Power budget parameters.

3.2 Radar Power Budget and Range Resolution Model

To estimate the detectability of space debris by a satellite-mounted radar system, the received power P_r from a target object is calculated using the monostatic radar range equation:

$$P_r = \frac{P_{\text{tx}} \cdot G_{\text{tx}} \cdot Code_{en} \cdot G_{\text{rx}} \cdot \lambda^2 \cdot \sigma}{(4\pi)^3 \cdot d^4}$$
(3.5)

where:

- $P_{\rm tx}$: Transmit power [W]
- $G_{\rm tx}, G_{\rm rx}$: Antenna gains (transmitter and receiver) [linear scale]
- $Code_{en}$: Coding gain [linear]
- λ : Wavelength [m]
- σ : Radar Cross Section (RCS) of the debris [m²]
- d: Distance between satellite and debris [m]

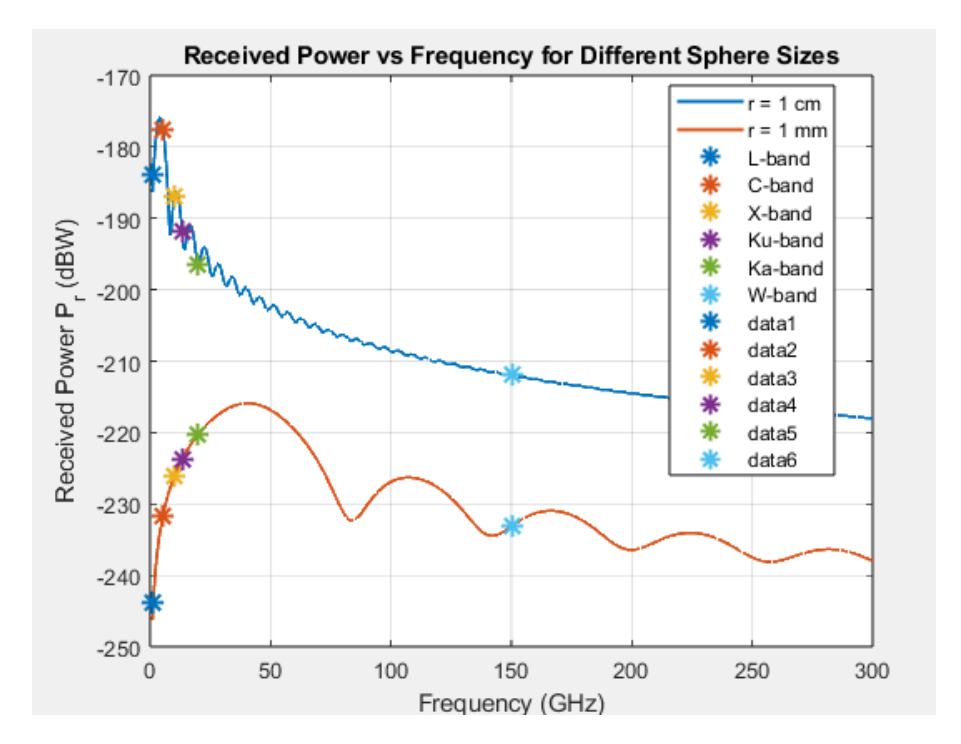


Figure 3.4: Received power variation as a function of frequency band for debris sizes 1 cm & 1 mm

This model assumes a **monostatic configuration**, which is justified by the fact that the transmitting and receiving subsystems are co-located on the same satellite. Since the debris-satellite distance is large (hundreds to thousands of kilometers), the physical separation between the antennas is negligible. The propagation loss follows a d^4 dependency typical of radar backscatter.

The received power is compared with the thermal noise floor, computed as:

$$P_n = k \cdot T \cdot B \tag{3.6}$$

where:

- $k = 1.380649 \times 10^{-23}$ J/K: Boltzmann constant
- T: System temperature [K]
- B: Receiver bandwidth [Hz]

Additionally, the system's **range resolution** is expressed as:

$$\Delta R = \frac{c}{2B} \tag{3.7}$$

where:

- ΔR : Range resolution [m]
- c: Speed of light [m/s]

Bistatic configuration is also considered, with different combinations of satellite constellation and ground-based radar. Recalling the Radar Equation for the Bistatic Configuration

$$P_r = \frac{P_{\text{tx}} \cdot G_{\text{tx}} \cdot Code_{en} \cdot G_{\text{rx}} \cdot \lambda^2 \cdot \sigma}{(4\pi)^3 \cdot d_{tx}^2 \cdot d_{rx}^2}$$
(3.8)

It is important to highlight how the distance is computed: \mathbf{d}_{tx} denotes the distance from the transmitter to the debris, while \mathbf{d}_{rx} represents the distance from the debris to the receiver. To avoid line-of-sight (LOS) blinding, it is necessary to ensure that the receiver is positioned at least $10 \cdot HPBW$ away from the main beam axis of the transmitting antenna.

3.2.1 Code Enhancement

A parameter named $Code_{en}$ has been considered in the previously discussed formulas for both the monostatic and bistatic cases. Since we can modulate a signal (whether it is a transmission, CW, or monopulse signal) in terms of amplitude, frequency, and phase, this parameter refers to the signal that is being used. When we code a signal, we generally increase the signal's signal-to-noise ratio (SNR) and the separation between the main and side lobes in comparison to the pure signal. The goal of this technique is to code the signal using a different phase, which increases the range resolution. Phase-Modulated Continuous Wave (PMCW) radar has emerged as a compelling alternative to the more traditional Frequency-Modulated Continuous Wave (FMCW) radar in various applications, including automotive sensing, industrial monitoring, defense, and security. PMCW radars transmit a continuous wave that is phase-modulated using predefined digital codes, often binary sequences such as Golay complementary codes or pseudorandom sequences. This modulation technique offers several distinct advantages that address important challenges in radar performance, hardware design, and coexistence in crowded electromagnetic environments.

Superior Range Resolution and Low Sidelobes

One of the most significant benefits of PMCW radar is its ability to achieve high contrast range resolution (HCR) while maintaining extremely low sidelobes in the radar's ambiguity function. Sidelobes are undesirable artifacts that can mask weaker targets or generate false detections. In FMCW systems, sidelobes typically remain at about -13 dB without heavy windowing, which reduces the mainlobe amplitude and effective resolution. In contrast, PMCW systems can employ carefully designed phase codes whose autocorrelation sidelobes are theoretically zero or extremely low (e.g., Golay codes can produce sidelobe levels below -40 dB). This allows PMCW radars to detect and distinguish multiple closely spaced targets with minimal interference from sidelobe leakage.

Improved Interference Resilience

Modern environments, such as highways or factory floors, often host numerous radars operating simultaneously. FMCW radars can experience significant mutual interference because their frequency sweeps overlap in time and frequency. PMCW mitigates this issue by encoding the transmit waveform with unique orthogonal or quasi-orthogonal codes. Since each radar operates with a different code, cross-correlation between signals from different systems is inherently low, reducing the probability of interference-induced false alarms or degraded sensitivity. This property makes PMCW an excellent candidate for applications requiring many radar units to coexist within a limited frequency band.

High Doppler Unambiguity and Velocity Performance

FMCW radars can suffer from Doppler ambiguities because frequency shifts due to target motion combine with the frequency sweep, complicating the estimation of velocity. PMCW radars, in contrast, can be designed to achieve high Doppler unambiguity without time-division multiplexing. The phase modulation is applied at a chip rate that does not interfere with Doppler shifts, and the transmitted waveform can be structured to allow clear separation of range and velocity information in the processing stage. As a result, PMCW radars are well-suited for detecting high-speed targets without requiring long observation times or complex de-aliasing algorithms.

Simplified Analog Front-End and Digital Processing

Another advantage of PMCW radar is the simplification of the analog front-end. Unlike FMCW radars, which need precise ramp generators, linear frequency modulation circuits, and analog mixing to perform stretch processing, PMCW radars transmit a constant carrier frequency and perform all modulation digitally. This approach reduces phase noise and spurious artifacts and simplifies the hardware implementation, making PMCW particularly attractive for CMOS integration. The received signal is typically digitized directly, and correlation processing is done entirely in the digital domain, enabling flexible reconfiguration and software-defined operation.

Seamless Integration with Communication Functions

PMCW systems lend themselves naturally to combined radar and communication functions. The use of spread-spectrum phase modulation techniques is conceptually similar to Code Division Multiple Access (CDMA) used in wireless communication. This allows a PMCW radar platform to multiplex radar sensing and data transmission in the same waveform, enabling new concepts such as joint radar-communication (JRC) systems that share spectrum resources efficiently. This integration supports emerging applications like vehicle-to-vehicle (V2V) and vehicle-to-everything (V2X) connectivity with minimal additional complexity.

Flexible Waveform Design and Adaptive Operation

Because PMCW radar relies on digital sequences, its waveform properties can be modified in software to adapt to different operating conditions or regulatory constraints. For example, different codes can be selected to optimize range resolution, improve clutter rejection, or enhance resilience against jamming. This flexibility enables dynamic reconfiguration of the radar's sensing performance without changing hardware, an increasingly important capability in environments with evolving threats or interference sources.

In summary, PMCW radar technology provides a powerful set of advantages: outstanding range resolution with low sidelobes, strong interference resilience, high Doppler unambiguity, simpler hardware design, potential for combined radar and communication functions, and reconfigurable waveform capabilities. As radar sensing proliferates in automotive, industrial, and security applications, PMCW is poised to become a preferred solution for demanding scenarios where performance, coexistence, and integration matter most. In this section the objective is to validate the value $Code_{ena} = 30 \ dBi$, so we simplify the validation and understand the gain obtained through phase modulation of a single rectangular pulse. We first generate a rectangular pulse as shown in Fig. ??. To phase-modulate the Pulse, we generate a Gold sequence of length $l = 2^n - 1$, with n = 10, by XOR-ing two maximum length sequences (m-sequences) defined by Linear Feedback Shift Registers (LFSRs). The generator polynomials are:

$$u(x) = x^{10} + x^3 + 1, (3.9)$$

$$v(x) = x^{10} + x^9 + x^8 + x^6 + x^3 + x^2 + 1, (3.10)$$

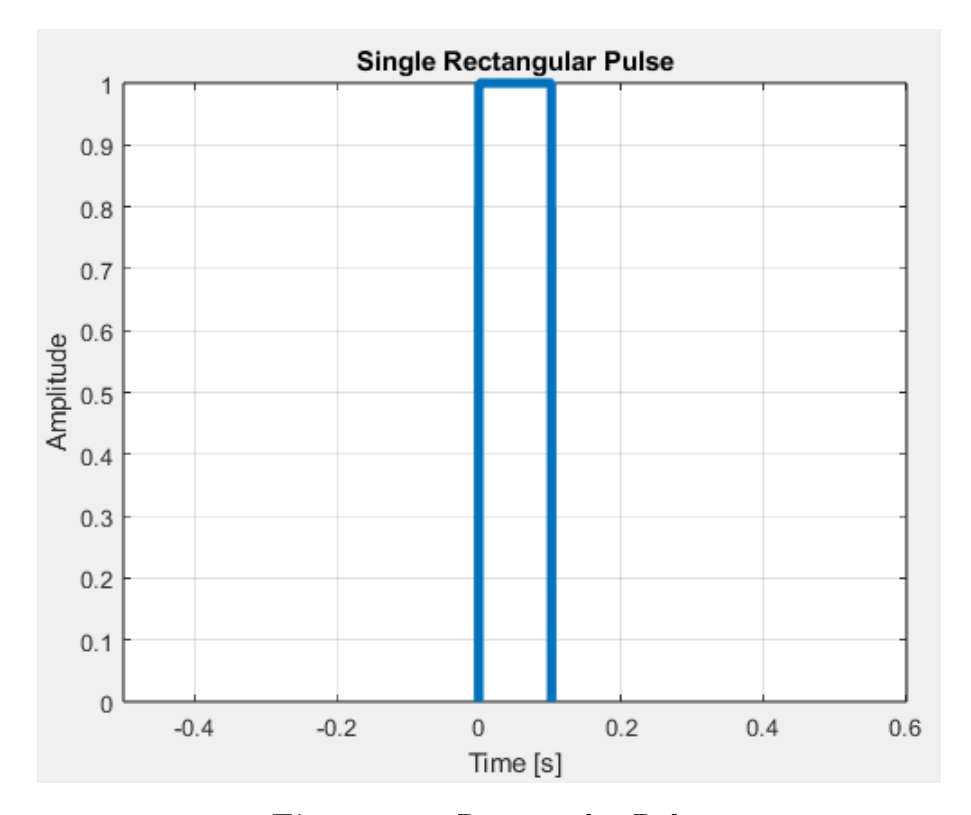


Figure 3.5: Rectangular Pulse

with identical initial states:

$$[1, 0, 0, 0, 0, 0, 0, 0, 0, 0]$$
.

The Gold sequence is obtained as the bitwise XOR of the two sequences:

$$G(k) = U(k) \oplus V(k), \qquad k = 0, 1, \dots, l - 1,$$
 (3.11)

where U(k) and V(k) are the outputs of the two LFSRs, and \oplus denotes modulo-2 addition. Mapping $\{0,1\} \to \{+1,-1\}$ gives the bipolar Gold sequence:

$$q(k) = 1 - 2 \cdot G(k). \tag{3.12}$$

Figure 3.6 shows the first 50 chips of the generated Gold sequence.

The Gold sequence is then embedded into the Rectangular pulse, the chip duration is:

$$T_c = \frac{T_s}{l}, \qquad T_s = \frac{1}{f_s}$$
 second.

Where T_s is the Pulse Duration. If we consider x[n] as the original signal and g[n] the gold sequence then the output signal obtained by the embedding of the two sequence is as follow:

$$y[n] = x[n] \cdot g[n] \tag{3.13}$$

This modulated pulse represented in 3.7

The resulting phase difference between the Pulse and the modulated signal is shown in Fig. 3.8.

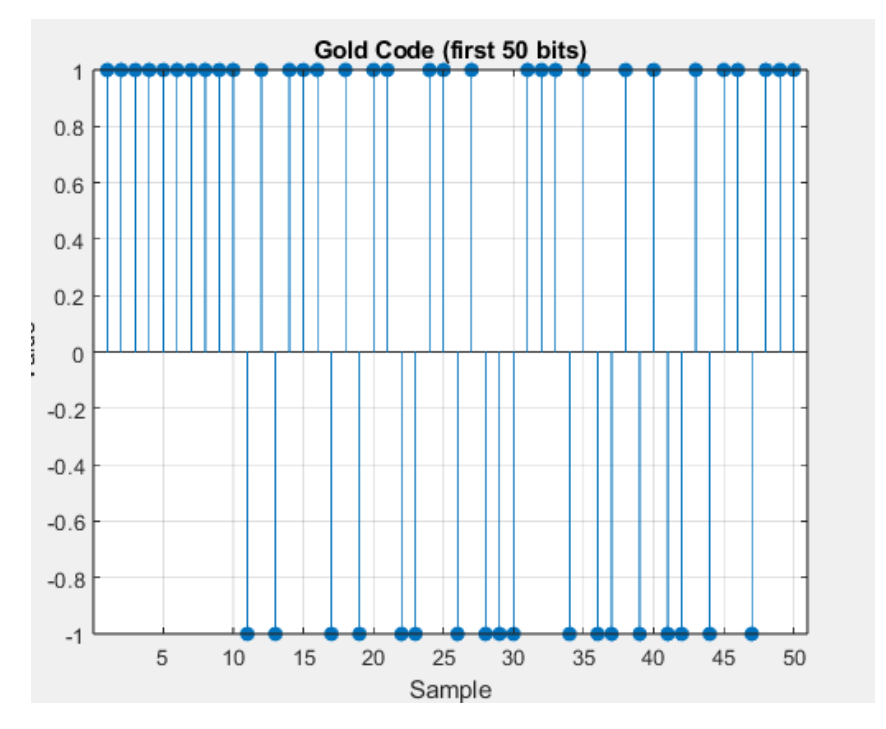


Figure 3.6: First 50 samples of the Gold Sequence

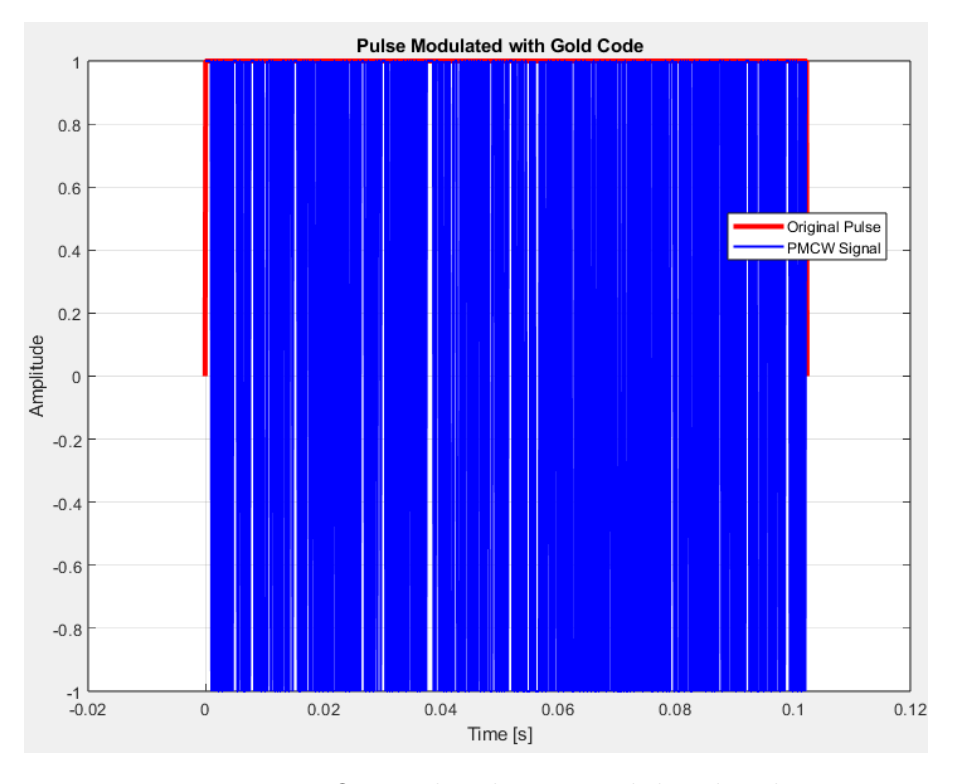
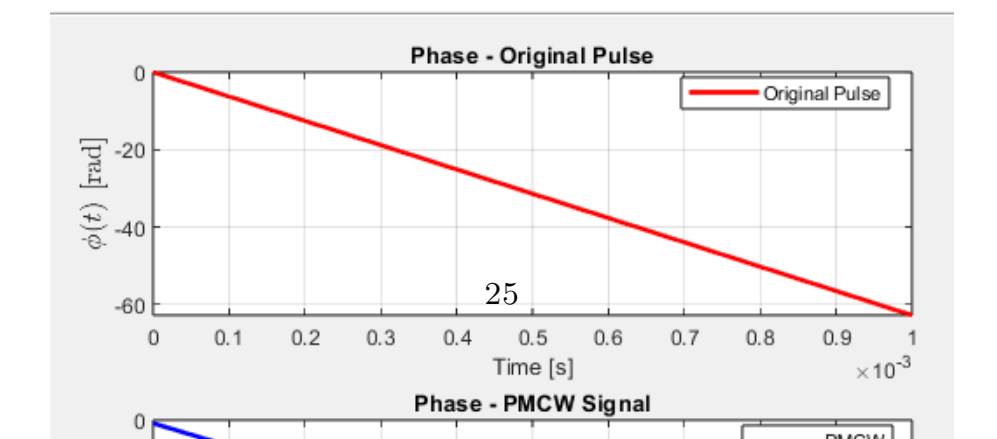


Figure 3.7: Original Pulse vs Modulated Pulse



By evaluating the normalized autocorrelation function, shown in Fig. 3.9, it is evident that the sidelobes are significantly reduced using PMCW. This improvement yields a **Code Enhancement Gain** of approximately:

 $G \approx 29.81 \text{ dB}.$

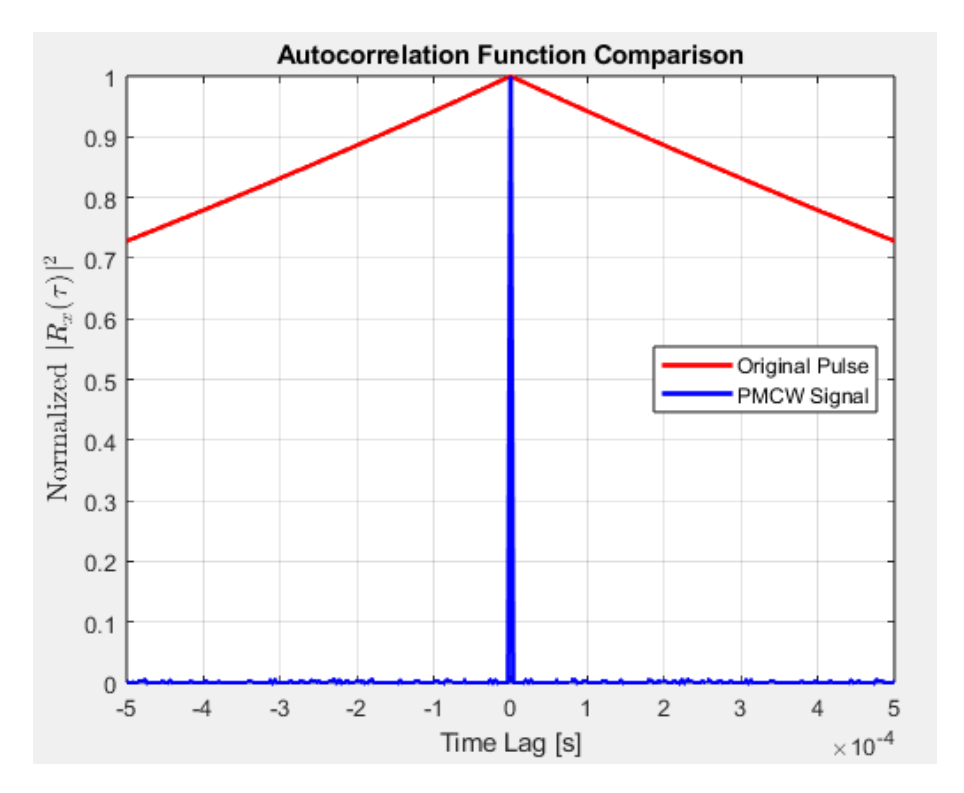


Figure 3.9: Normalized Autocorrelation function for MonoPulse and Modulated Pulse

3.3 Scenario

Even if the detection is analyzed always in the same manner, between the Monostatic and Bistatic cases there are some difference. In all the Monostatic setup the geometry is always the same, the only difference is obviously when transmitting from the ground segment, which is on the earth so it is placed under the Region of interest, while for satellites, the transmission is from above the Region of Interest.

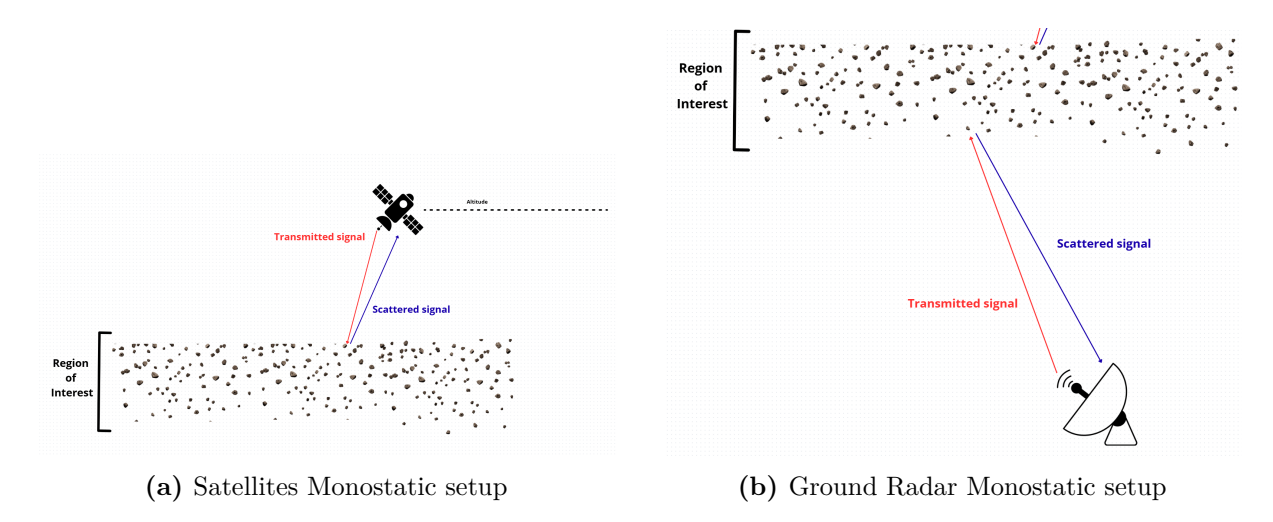


Figure 3.10: Comparison between Monostatic setups: (a) Satellite and (b) Ground Radar

Differently, for the Bistatic cases we can group the scenario based on where the TX and RX are placed :

- 1. Transmitter above the Region of interest' orbit & Receiver lower than the ROI orbit : $IRIS^2 like$ high orbit / $IRIS^2 like$ low orbit, METOP-SG / $IRIS^2 like$ low orbit , HY-2 / $IRIS^2 like$ low orbit
- 2. Transmitter on Earth, so lower than the ROI orbit & Receiver higher than the ROI orbit: TIRA / $IRIS^2 like$ high orbit, HUSIR / $IRIS^2 like$ high orbit.

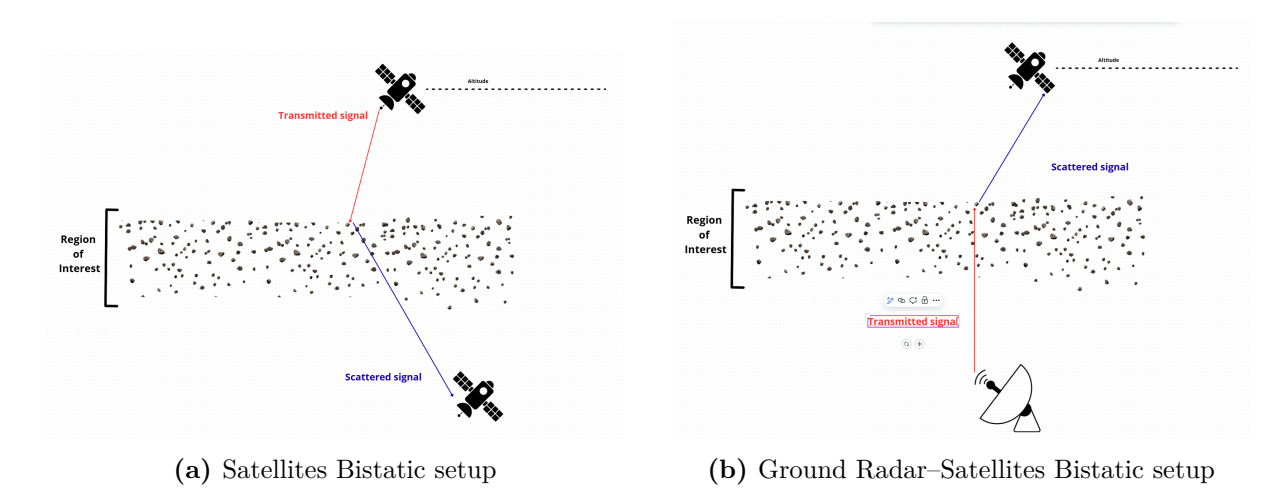


Figure 3.11: Comparison between Bistatic setups: (a) Satellite and (b) Ground Radar–Satellite

3.4 Monostatic

In the following analysis the first plot shows the received power as a function of distance for different debris sizes, compared to the noise floor at various bandwidths. This allows an evaluation of the maximum detection range under different resolution configurations. The second plot represents the achievable range resolution versus distance, indicating the capability of detecting and resolving small objects (e.g. 1 mm or 1 cm) in the orbital environment.

3.4.1 $IRIS^2$ -like high

Parameters and Results

The $IRIS^2$ -like constellation is assumed to be deployed at two different altitudes: the primary layer at approximately 1200 km, and a secondary layer consisting of a few satellites at altitudes between 450 km and 700 km. In this work, we consider a monostatic configuration for the higher-altitude satellites, as the lower orbit lies below the region of interest for detecting Low-Numbered Trackable (LNT) debris, which typically resides between 800 km and 1000 km. The concept involves using a receiver onboard the same satellite to capture the backscattered signal from the targeted debris. The table 3.3 shows the parameters used for the analysis in the radar equation.

Parameters	Value	Source
Altitude	1200 km	spacenews [11]
Carrier Frequency	20/12 GHz	spacenews [11]
Transmit Power	1 W	Transmit dual polarised antenna [12]
Antenna Gain TX	36 dBi	Transmit dual polarised antenna [12]
Antenna Gain RX	30 dBi	Assumed

Table 3.3: Simulation parameters and corresponding sources.

In this study, two frequency bands are considered, namely 20 GHz and 12 GHz, in order to explore a more realistic scenario. This choice reflects the fact that different frequency ranges may be employed depending on whether the transmitted signal is intended for communication or radar applications.

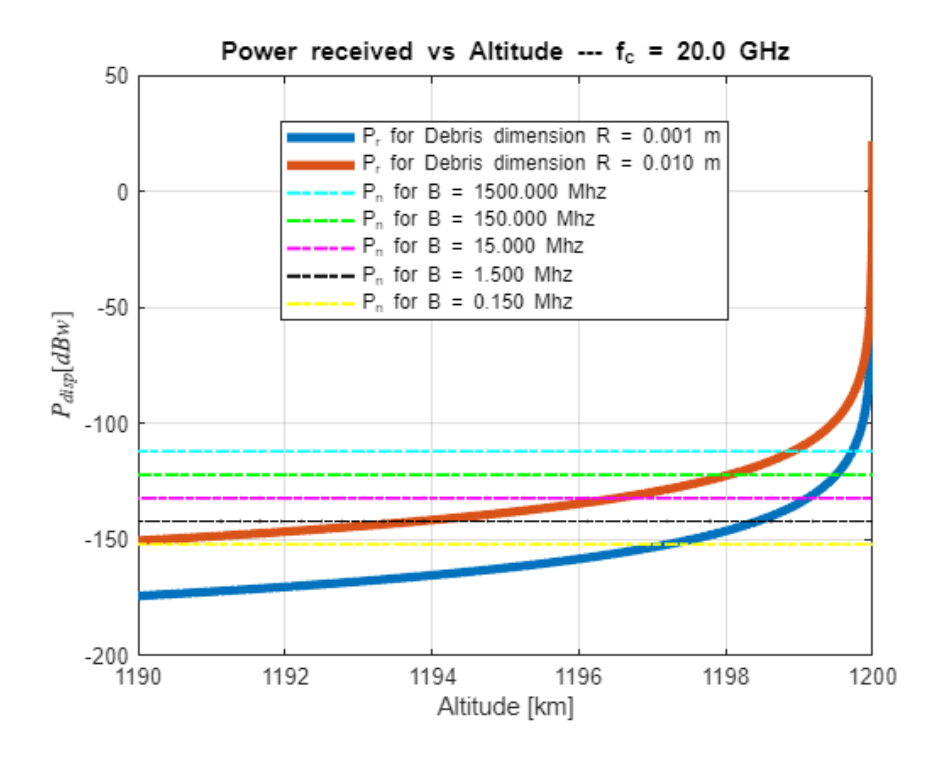


Figure 3.12: Received Power for $f_c = 20 \text{ GHz}$

The first image (3.12) illustrates the received power as a function of altitude (in meters). In this analysis, the transmitter gain is assumed to be 36 dB, representing the lowest considered value and therefore a worst-case scenario, while the receiver, equipped with a different antenna, has a gain of 30 dB. Under these conditions, the distance at which debris can be detected is relatively limited compared to the available bandwidth. It is important to note that, at this preliminary stage, the analysis does not account for range resolution, but rather focuses on evaluating the detection capability of the system. Afterward, further considerations can be made by including additional factors.

Figure 3.13 illustrates the impact of different bandwidths on **resolution**, while the **range** indicates the maximum detectable distance for the specified object. What is possible to observe from the above figure is that:

- For the Blue line (1 mm debris size) by increasing the frequency from 12 GHz to 20 GHz the MDR increase
- $\bullet\,$ For the Orange line (1 cm debris size) an increase of the frequency lead to a decrease of the MDR

This behavior is related to the RCS and it can be seen from the figures 3.3b and 3.3a since the region at which the two frequency band change based on the size of the object. In fact while for the RCS of the 1-mm debris an increase of the band leads to higher value of the RCS, since we are still in the Rayleagh Region, i.e in the exponential behavior of the function, for the 1-cm debris the ka-band reach lower value with respect to the X-band. Except for the fact that this behavior in the MDR shows that the RCS has an high impact on the received power, P_R , another consideration to make is the trade-off between the Range Resolution and the MDR values, in this case for both the debris sizes the MDR values are much lower w.r.t the Range Resolution leading to the consideration that we could detect those debris only few km away from the satellite with high value of Range Resolution, up to 1 km. This brings to the finding that this option is not optimal.

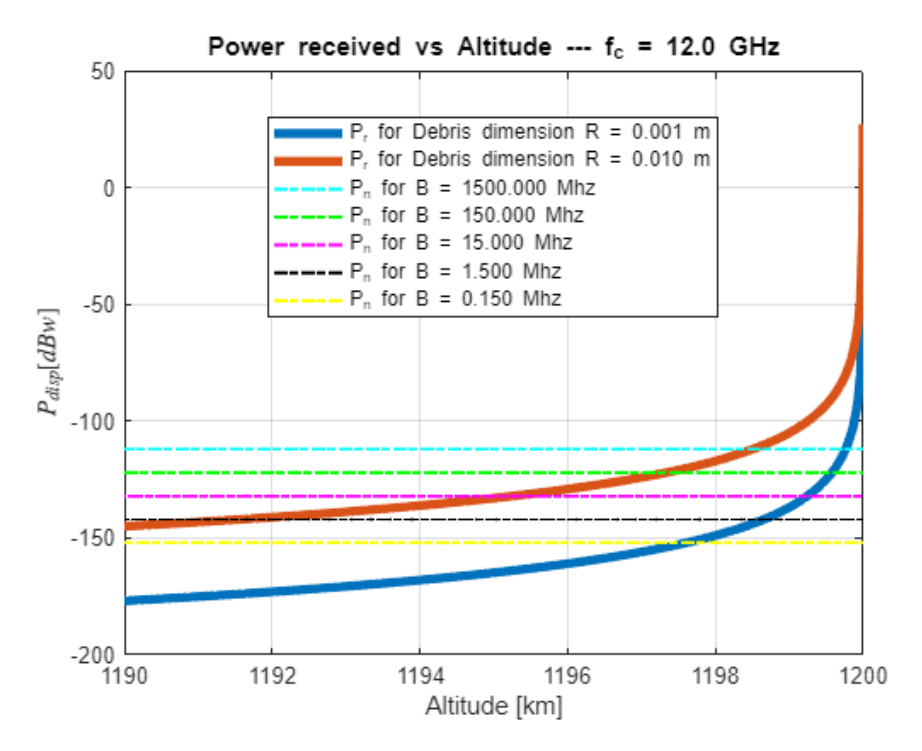


Figure 3.13: Received Power for $f_c = 12 \text{ GHz}$

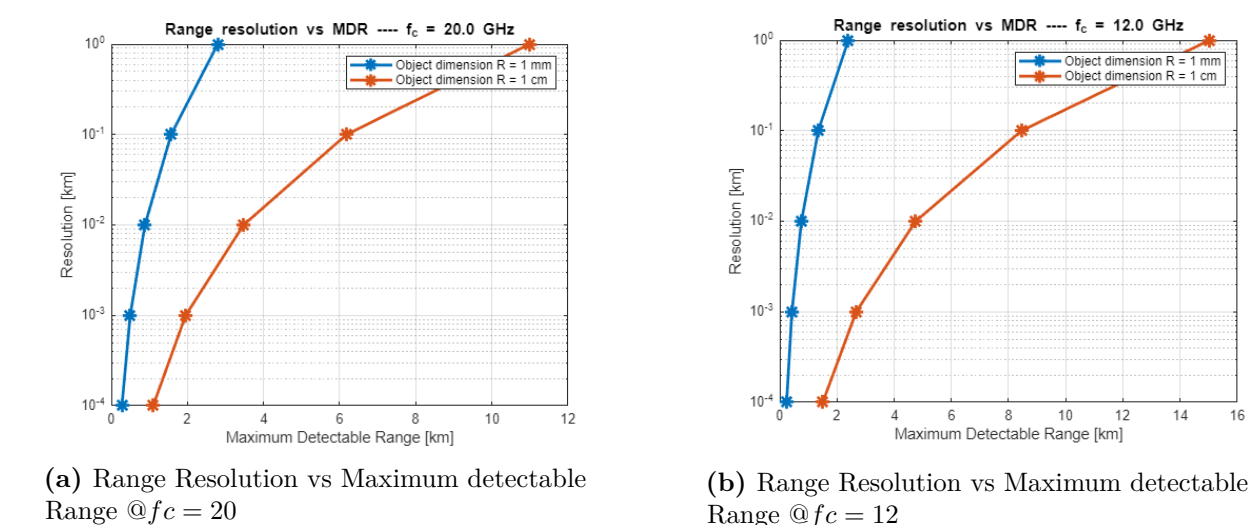


Figure 3.14: Range Resolution vs Maximum detectable Range Comparison

Range @fc = 12

14

3.4.2 METOP - sg

Metop-SG (Meteorological Operational Satellites – Second Generation) is a series of six meteorological satellites developed by EUMETSAT and the European Space Agency, scheduled for launch between 2025 and 2039.

These satellites are part of EUMETSAT's Polar System – Second Generation (EPS-SG) program, dedicated to weather forecasting and climate monitoring from polar orbit, as a continuation of the EUMETSAT Polar System (EPS). They are also included in the Joint Polar System (JPS), a collaborative program between EUMETSAT and the United States' NOAA.

The constellation comprises two types of satellites, Metop-SGA and Metop-SGB, which differ in terms of the scientific instruments they carry. They operate in a polar orbit at an altitude of approximately 832 km, each completing about 14 orbits per day.

Parameters and Results

The Metopp-SG have many instruments on-board, such as scatterometer, altimeter and different type of radar that depends on the application, the rational behind the choice of the scatterometer for this analysis is that it has the highest power and gain, this rational is kept even for the other satellites. While for $IRIS^2$ -like satellites we considered two antennas, one for transmission the other as receving, here and for the already existing constellation and ground radar the same antenna has been considered as transmitting and receiving, this is due to the fact that those are already deployed and changing the architecture of the satellite/ground radar is difficult. This is the reason why the central frequency and the number of antennas is different from the $IRIS^2$ -like satellites.

Parameters	Value	Source
Altitude	835 km	Space Oscar[13]
Carrier Frequency	5,225 GHz	Space Oscar[13]
Transmit Power	540 W	Space Oscar [13]
Antenna Gain TX	39.61 dBi	EOportal [14]
Antenna Gain RX	39.61 dBi	EOportal [14]

Table 3.4: Simulation parameters and corresponding sources.

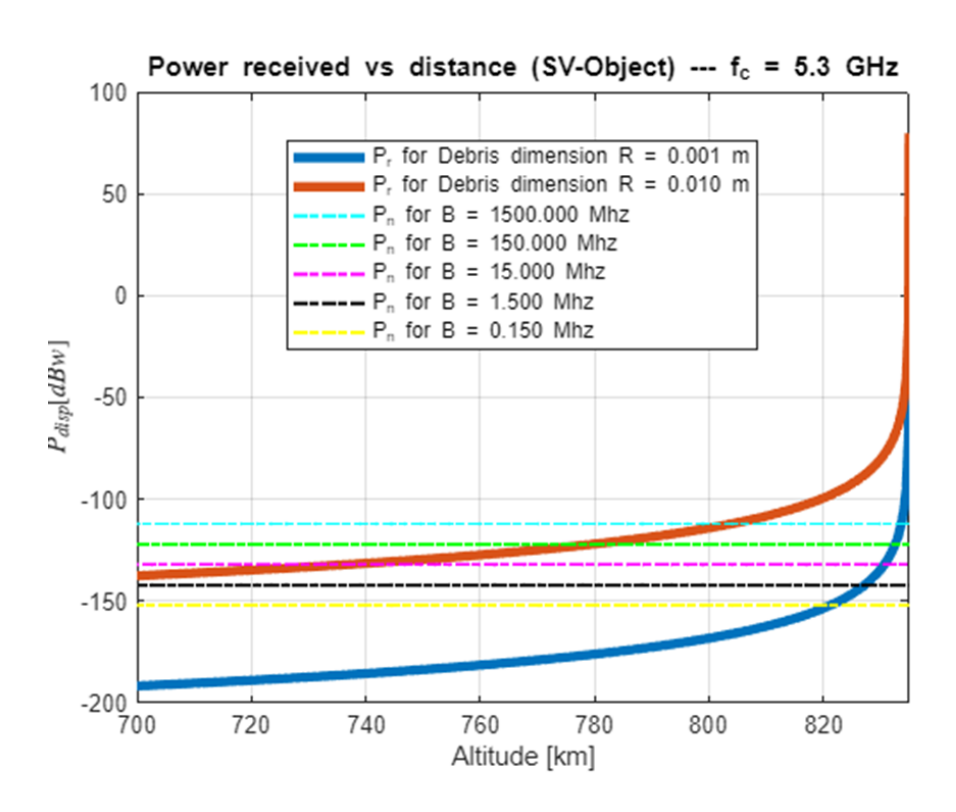


Figure 3.15: P_R vs altitude - METOP SG Monostatic

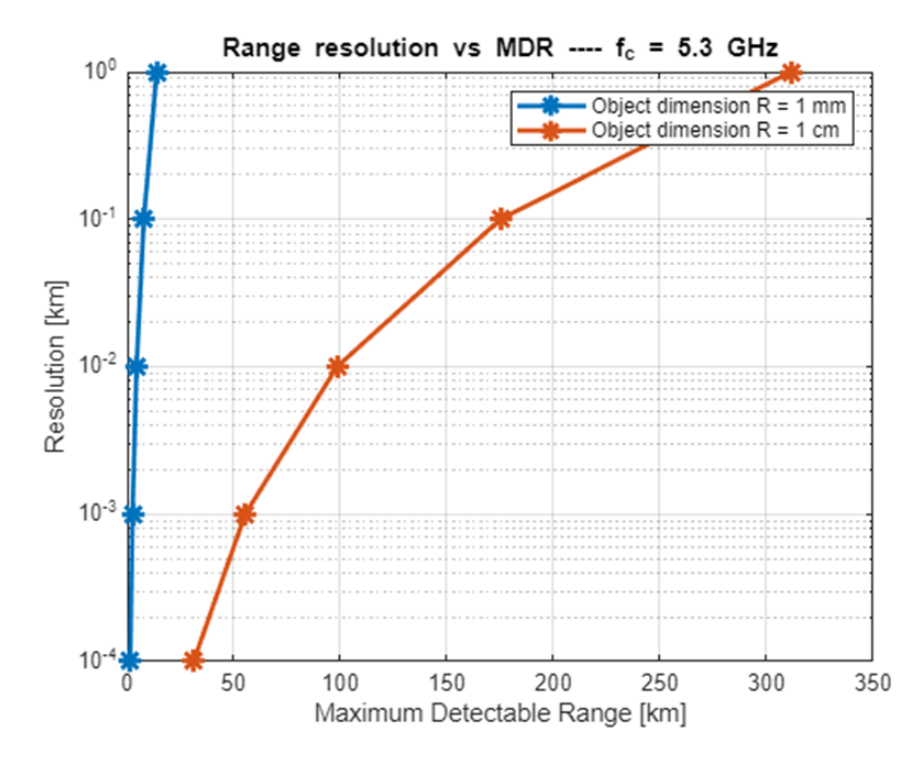


Figure 3.16: Range Resolution vs Maximum Detectable Range- METOP SG Monostatic

Considering the values of the antenna taken in [14] with respect to the previous case independently from the RCS the Maximum Detectable Range is higher reaching up to 330 km for 1-cm debris and 20 km for 1-mm debris, anyway even in this case those values are reached for 1 km Range Resolution making this option hard to use for in-space detection.

3.4.3 HY - 2

The Haiyang-2 (HY-2) satellite series, developed by China for oceanographic applications, is equipped with a Ku-band scatterometer designed to provide global, all-weather measurements of sea surface wind speed and direction through the retrieval of sigma-0 backscatter values. Offering a spatial resolution of approximately 25 km and achieving accuracies of about ± 2 m/s for wind speed and $\pm 20^{\circ}$ for wind direction, the HY-2 scatterometer constitutes a reliable data source for the study of marine meteorology and ocean circulation, particularly under moderate wind conditions. In the context of this thesis, the analysis explicitly takes into account the wind parameters derived from the scatterometer from HY2.

Parameters and Results

Parameters	Value	Source
Altitude	937 km	Space Oscar[15]
Carrier Frequency	13,256 GHz	Space Oscar[15]
Transmit Power	120 W	Space Oscar [16]
Antenna Gain TX	41.59 dBi	[16]
Antenna Gain RX	41.59 dBi	[16]

Table 3.5: Simulation parameters and corresponding sources.

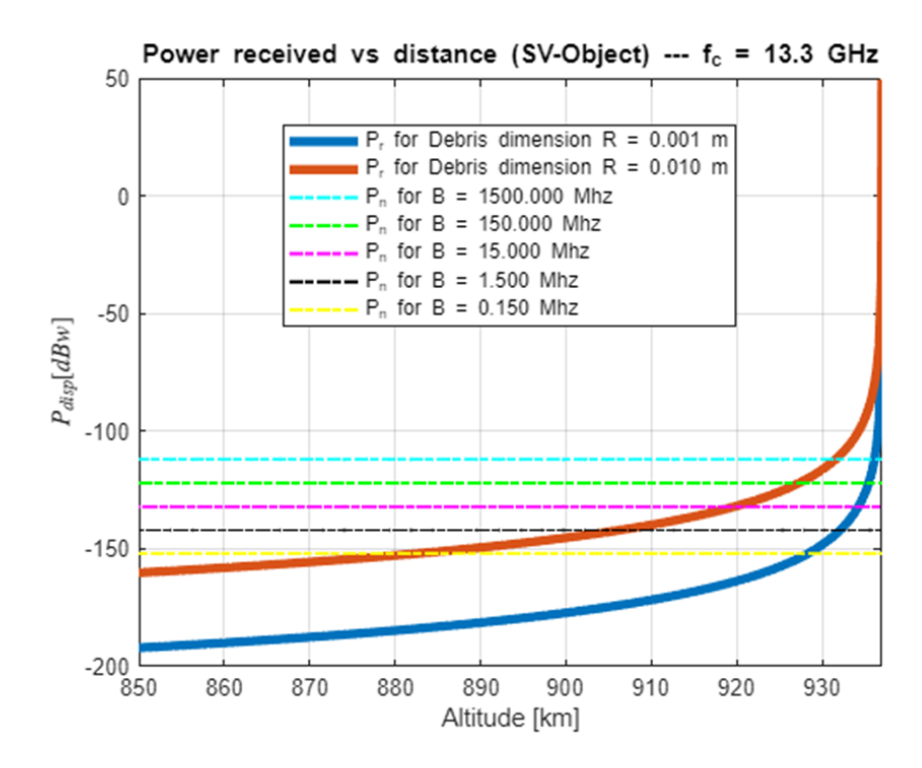


Figure 3.17: P_R vs altitude - HY2 Monostatic

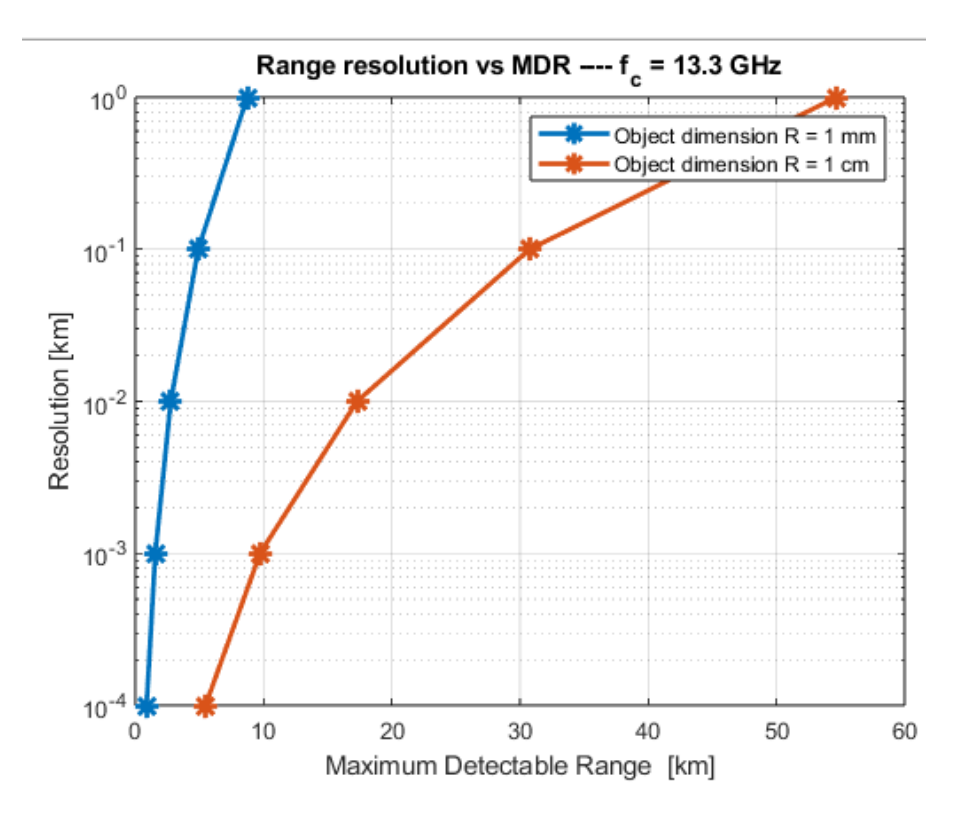


Figure 3.18: Range Resolution vs Detection Range Limit - HY2 Monostatic

The last constellation under analysis shows, from Figs. 3.17 and 3.18, intermediate results even if in overall the equipment has higher values of Gain G, and Transmitting power P_t , this is mostly due to the RCS that lead the constellation to have worse results than the most performing constellation analyzed up to now which is the METOP-SG.

3.4.4 *TIRA*

The Tracking and Imaging Radar (TIRA), operated by the Fraunhofer Institute for High Frequency Physics and Radar Techniques (FHR) in Germany, is one of the most advanced ground-based radar systems worldwide for space surveillance and research. Located in Wachtberg, it features a fully steerable 34-meter parabolic antenna equipped with a high-power L-band (1.333 GHz) tracking radar and a Ku-band (16.7 GHz) imaging radar. This dual-frequency configuration enables TIRA to perform both precise tracking of satellites and space debris and high-resolution imaging, with the Ku-band providing detailed radar images of objects in low Earth orbit. The system plays a critical role in monitoring space debris, characterizing satellites, and supporting collision risk assessment, making it a key European asset for space situational awareness.

Parameters	Value	Source
Altitude	0 km - On earth	Fraunhofer[17]
Carrier Frequency	1,33 GHz	Fraunhofer [17]
Transmit Power	1-2 MW	Fraunhofer[17]
Antenna Gain TX	49.53 dBi	Fraunhofer[17]
Antenna Gain RX	49.53 dBi	Fraunhofer[17]

Table 3.6: Simulation parameters and corresponding sources.

Parameters and Scenario

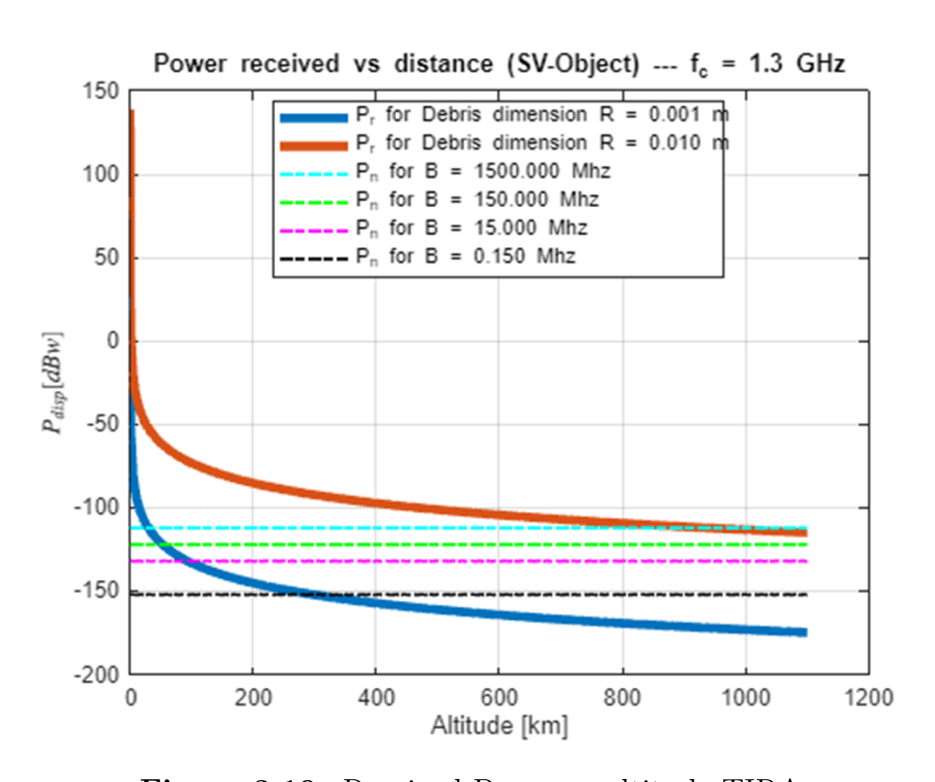


Figure 3.19: Received Power vs altitude-TIRA

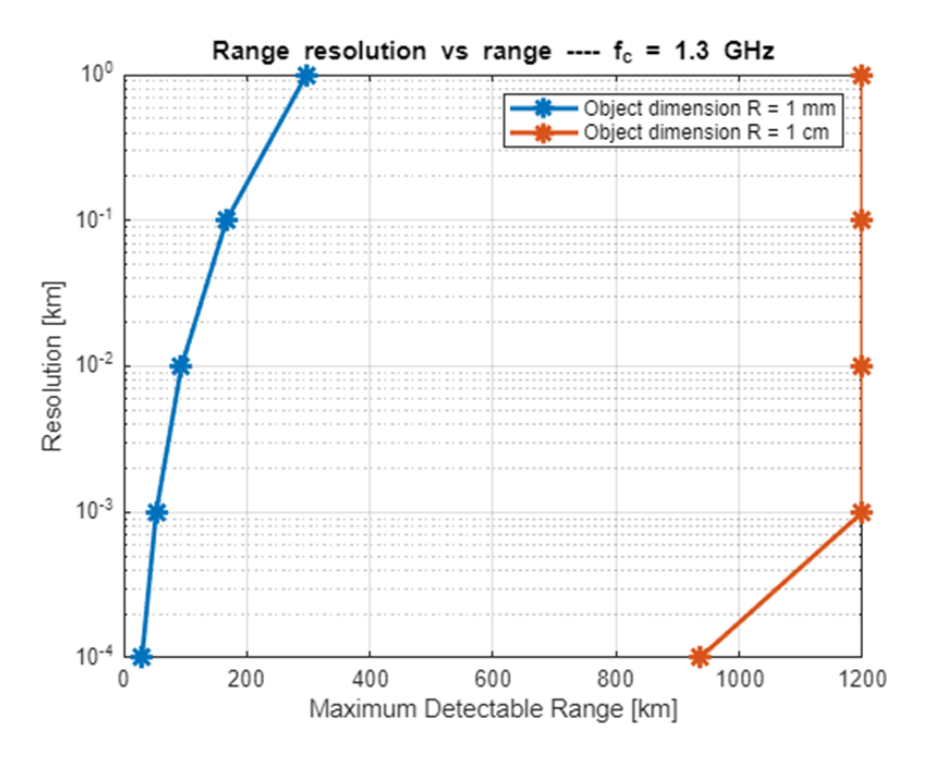


Figure 3.20: Range Resolution vs Detection Range Limit - TIRA

Comparing the results obtained until now, it becomes clear that the capability of the monostatic setup on-board of the aformentioned satellites constellation is limited. From the Received power compared to the Noise level in fig. 3.19 and the **Maximum Detectable Range** in 3.20, what can be depicted is that the system's capability from the ground is much higher since there are no limitations for what concern weight, dimension and therefore the system parameters. Even if TIRA work at the **L-BAND** it allows to detect debris up to:

• 1 cm : 1100 km

• 1 mm : 230 km

3.4.5 *HUSIR*

The Haystack Ultrawideband Satellite Imaging Radar (HUSIR) is a high-resolution ground-based radar system operated by MIT Lincoln Laboratory for the U.S. Space Surveillance Network. Upgraded from the original X-band Haystack Long-Range Imaging Radar (LRIR) beginning in 2010 and fully operational in 2014, HUSIR combines X-band (10 GHz, 1 GHz bandwidth) and W-band (92–100 GHz, 8 GHz bandwidth) capabilities, enabling image resolutions as fine as 3 cm and satellite tracking accuracy down to 0.0005°. It can characterize orbital debris as small as 5 mm in low Earth orbit, providing critical data to the NASA Orbital Debris Program Office for modeling the debris environment and assessing risk

Parameters	Value	Source
Altitude	0 km - On earth	NASA [18]
Carrier Frequency	10 GHz	NASA [18]
Transmit Power	$250~\mathrm{KW}$	NASA [18]
Antenna Gain TX	67.23 dBi	NASA [18]
Antenna Gain RX	67.23 dBi	NASA [18]

Table 3.7: Simulation parameters and corresponding sources.

Parameters and Scenario

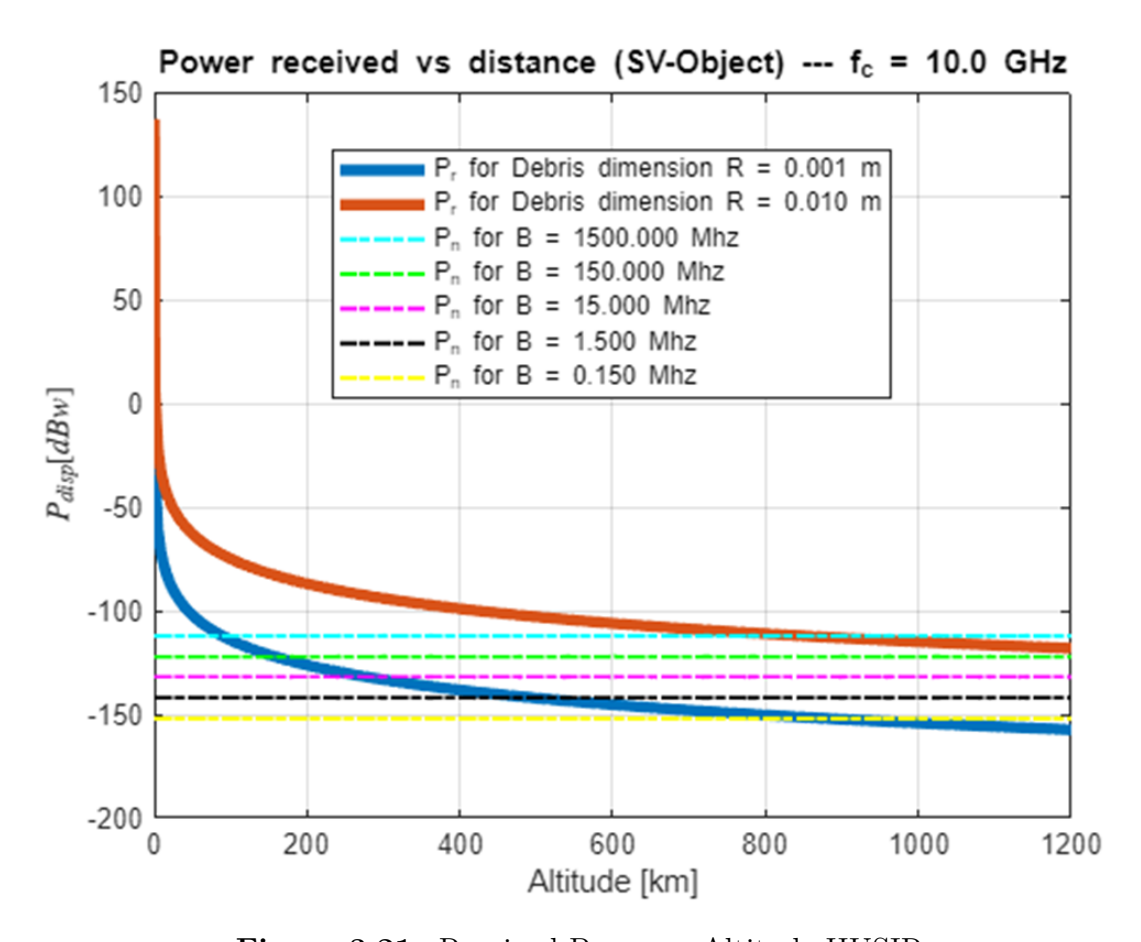


Figure 3.21: Received Power vs Altitude-HUSIR

Already from the TIRA we stated that ground RADAR have higher performance, with the monostatic approach HUSIR demonstrate the highest performance, allowing for a full detection of 1-cm debris already with Range Resolution $\Delta R = 1$ m and up to 850 km with $\Delta R = 1$ km, in this case we can consider acceptable those values since the Maximum Range at which the detection can occur is way higher than the Range Resolution.

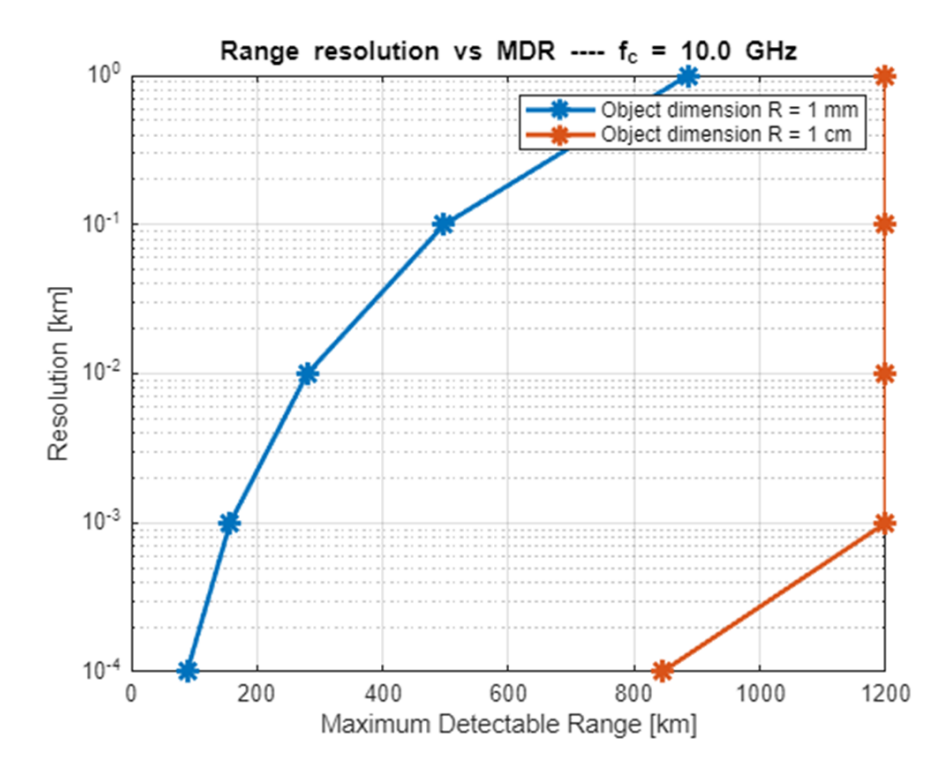


Figure 3.22: Range Resolution vs Detection Range Limit - HUSIR

3.5 Bistatic setup

A comparative analysis of the radar equation under identical parameters for monostatic and bistatic configurations was performed. The results, shown in Fig. 3.23, indicate that the monostatic setup provides higher received power at short ranges due to the single-antenna geometry and the d^{-4} dependence of the radar equation, but this power decays rapidly with distance. Conversely, the bistatic configuration, while exhibiting lower received power at close range because of the transmitter–receiver separation and geometric factors, maintains a slower decay at longer ranges. Beyond the crossover distance — the range at which the received powers from both configurations are equal — the bistatic configuration becomes advantageous.

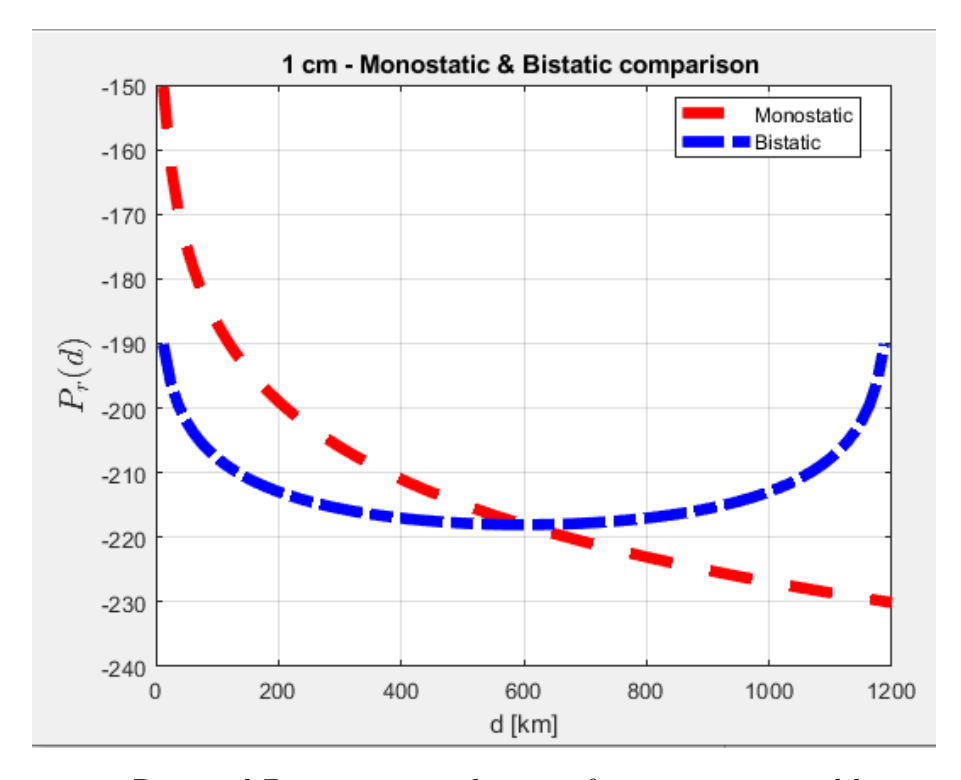


Figure 3.23: Received Power against distance for monostatic and bistatic setup

The crossover point depends on the system geometry and parameters such as antenna beamwidth and operational wavelength. In practical applications, monostatic radars benefit from simpler implementation and synchronization, whereas bistatic systems require more complex coordination but can extend coverage and improve detection performance at longer ranges. But something to highlight is that w.r.t the monostatic setup there are some consideration to be done:

- - We have to ensure that the backscattered signal from the debris should not be blinded at the RX side by the Line-of-Sight
- The geometry should change and the symmetry of the presented results shown in fig.3.23 needs some adjustment.

So let's assume that in order to satisfy those requirements we need to set the RX at a certain angle w.r.t to the TX beam, here we have to do some assumption since a lot of antenna exist and they have different pattern so we do the following assumption:

- We set the receveing satellite at an angle $\alpha = HPBW/2$, where **HPBW** is the Half Power Beam Width
- The Half Power Beam width is computed as for an aperture antenna $HPBW = \frac{70 \cdot \lambda}{Antenna_dim}$, the greatest dimension is considered for the computation

By these consideration the scenario becomes as follow in fig.3.24

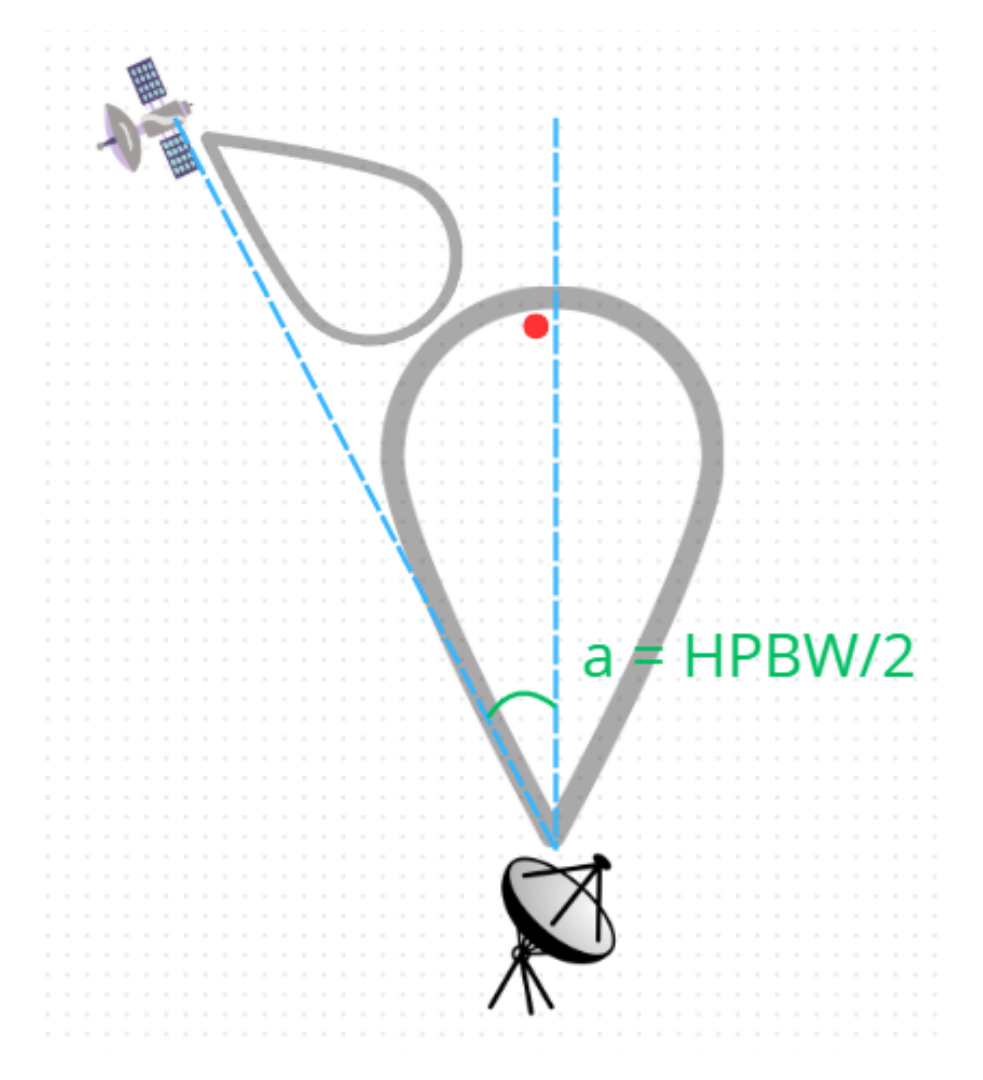


Figure 3.24: Bistatic scenario

Here in order to obtain reasonable results a function that computes the distance based on the aformentioned approach has been created and then validated. In this work, the distance between the debris object and the receiver is computed while accounting for the antenna beamwidth and a safety angular margin to mitigate line-of-sight (LoS) blinding effects. The first step involves the estimation of the Half-Power Beamwidth (HPBW), which represents the angular width of the main radiation lobe between the -3 dB power points. For an aperture antenna, an empirical approximation is expressed as

HPBW [°] =
$$\frac{70 \cdot \lambda}{\text{Antenna dim}}$$
,

where λ denotes the wavelength and Antenna_dim the effective aperture dimension of the antenna, both expressed in meters. To ensure that the debris lies outside the region of strong direct-path signals, a safety margin angle α is introduced, defined by

$$\alpha = 10 \cdot \text{HPBW}.$$

Based on this angular margin, the effective baseline between the transmitter (Tx) and receiver (Rx) is adjusted according to

$$D = \frac{\text{max_distance}}{\cos\left(\frac{\alpha}{2}\right)},$$

where max_distance corresponds to the actual Tx-Rx separation. Finally, the distance between the debris object and the receiver, d_{rx} , is determined using the law of cosines as

$$d_{\rm rx} = \sqrt{d_{\rm tx}^2 + D^2 - 2 d_{\rm tx} D \cos\left(\frac{\alpha}{2}\right)},$$

where d_{tx} denotes the distance from the transmitter to the debris. This formulation ensures that the receiver-debris distance is evaluated by incorporating both the antenna radiation pattern constraints and the imposed safety angular separation. The Compute_distance function was validated by comparing its output to a direct geometric calculation of the debris-receiver distance. The validation scenario considers a transmitter (Tx) and a receiver (Rx) separated by a baseline distance max_distance = 1200 km, with the Tx located at coordinates (0,0) and the Rx at (max_distance,0). The antenna aperture dimension was set to Antenna_dim = 1 m and the wavelength to $\lambda = 0.03$ m.

A set of 20 equally spaced transmitter–debris distances, $d_{\rm tx}$, was generated in the range from 0 to max_distance. For each value of $d_{\rm tx}$, the Half-Power Beamwidth (HPBW) was first computed as

$$\text{HPBW } [^{\circ}] = \frac{70 \cdot \lambda}{\text{Antenna dim}},$$

and the safety angular margin was obtained from

$$\alpha = 10 \cdot \text{HPBW}.$$

The effective baseline length D was then calculated using

$$D = \frac{\text{max_distance}}{\cos\left(\frac{\alpha}{2}\right)},$$

allowing the debris coordinates to be defined as

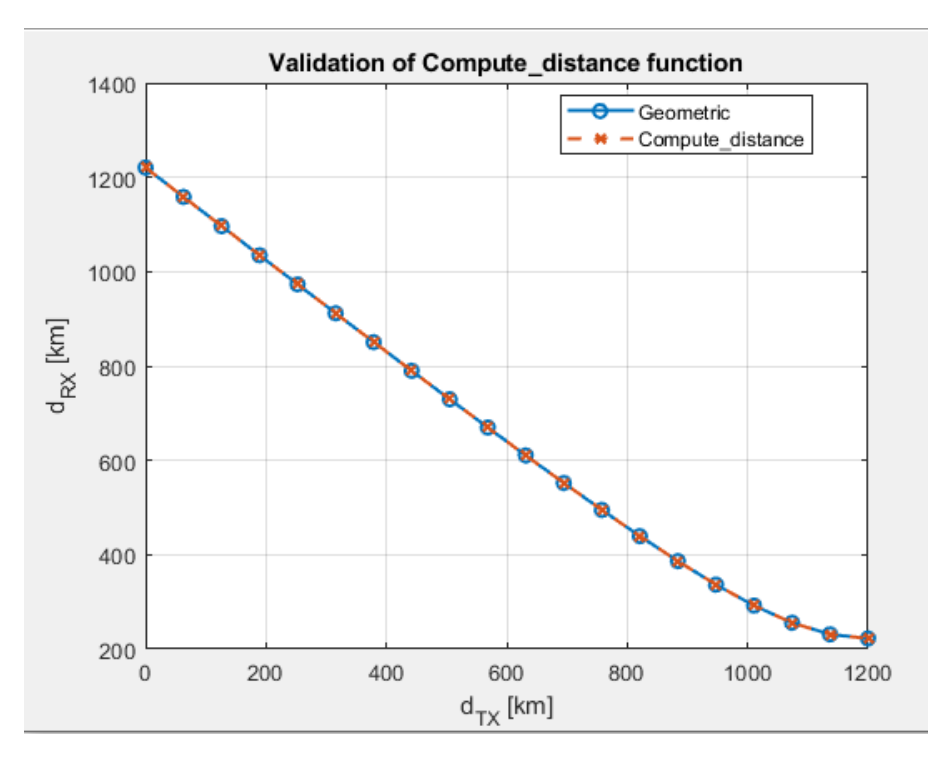
$$\mathbf{p}_{\text{debris}} = \left[d_{\text{tx}}, \ D \cdot \sin\left(\frac{\alpha}{2}\right) \right].$$

The debris–receiver distance, denoted $d_{\text{rx,geom}}$, was obtained as the Euclidean norm between the receiver coordinates and $\mathbf{p}_{\text{debris}}$.

In parallel, the same $d_{\rm tx}$ values were processed using the Compute_distance function to produce $d_{\rm rx,func}$. The two results were compared both numerically, via a table listing $(d_{\rm tx}, d_{\rm rx,geom}, d_{\rm rx,func})$, and visually, through a plot of $d_{\rm rx}$ as a function of $d_{\rm tx}$. The overlap between the geometric computation and the function output in fig 3.26confirmed the correctness of the implementation.

d_tx_m	d_rx_geom_m	d_rx_func_m
0	1.2204e+06	1.2204e+06
63158	1.1584e+06	1.1584e+06
1.2632e+05	1.0965e+06	1.0965e+06
1.8947e+05	1.0347e+06	1.0347e+06
2.5263e+05	9.7312e+05	9.7312e+05
3.1579e+05	9.1175e+05	9.1175e+05
3.7895e+05	8.5064e+05	8.5064e+05
4.4211e+05	7.8985e+05	7.8985e+05
5.0526e+05	7.2947e+05	7.2947e+05
5.6842e+05	6.6959e+05	6.6959e+05
6.3158e+05	6.1038e+05	6.1038e+05
6.9474e+05	5.5205e+05	5.5205e+05
7.5789e+05	4.949e+05	4.949e+05
8.2105e+05	4.3939e+05	4.3939e+05
8.8421e+05	3.8625e+05	3.8625e+05
9.4737e+05	3.3658e+05	3.3658e+05
1.0105e+06	2.9217e+05	2.9217e+05
1.0737e+06	2.5577e+05	2.5577e+05
1.1368e+06	2.312e+05	2.312e+05
1.2e+06	2.2241e+05	2.2241e+05

Figure 3.25: Distance Tx-debris, and results for Distance Rx-debris for norm and function



 $\textbf{Figure 3.26:} \ \, \textbf{Tx-debris distance from norm and compute distance function} \\$

3.5.1 $IRIS^2(highorbit) : TX - IRIS^2(loworbit) RX$

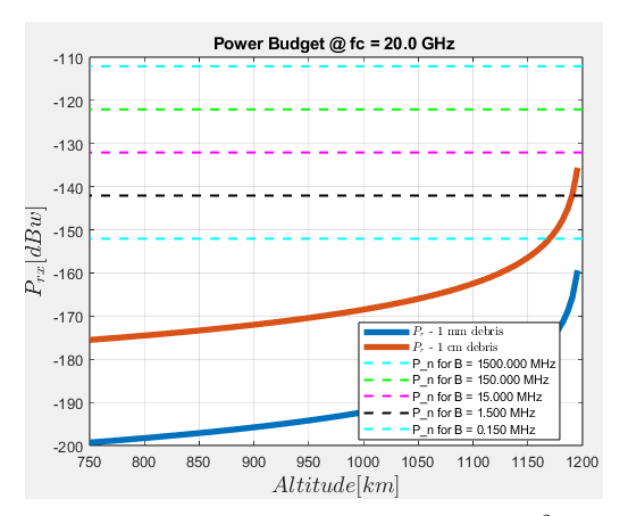
The first combination of satellites considered are the $IRIS^2$ constellations deployed at 1200 km and 750 km, here is assumed that those at higher altitude are transmitting while those in lower orbit are receiving the backscattered signal.

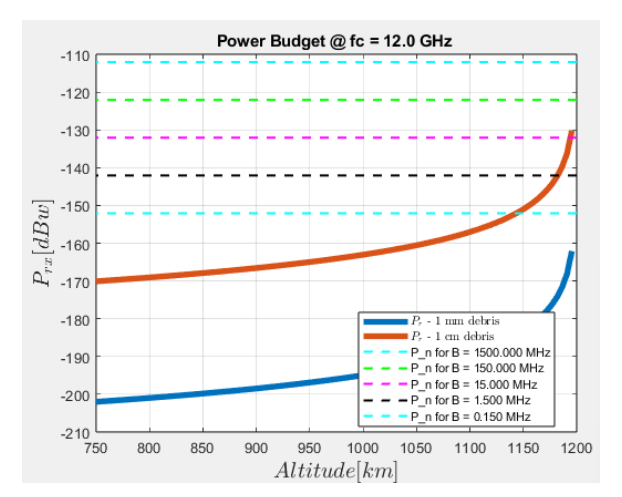
Parameters and Results

Parameters	Value	Source
Altitude	750 - 1200 km	[11]
Carrier Frequency	$20/12~\mathrm{GHz}$	Assumed
Transmit Power	1 W	Assumed
Antenna Gain TX	36 dBi	[12]
Antenna Gain RX	30 dBi	Assumed

Table 3.8: Simulation parameters and corresponding sources.

Using Ka Band From the results, in both configuration the 1-mm debris cannot be





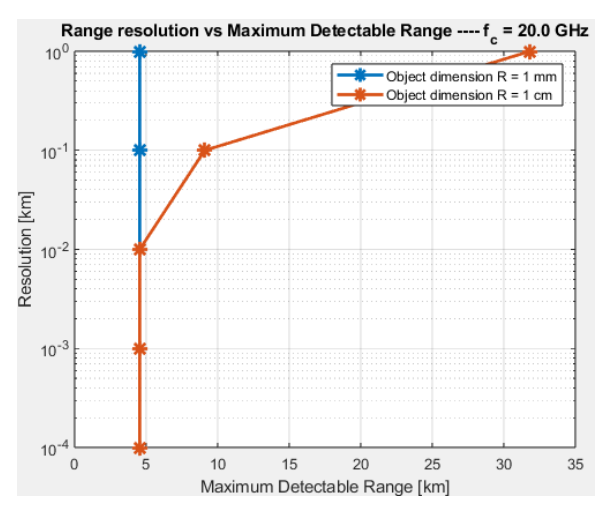
(a) Received Power vs Altitude - Tx: $IRIS^2$ -like high orbit / Rx: $IRIS^2$ -like low orbit @ $f_c = 20$ GHz

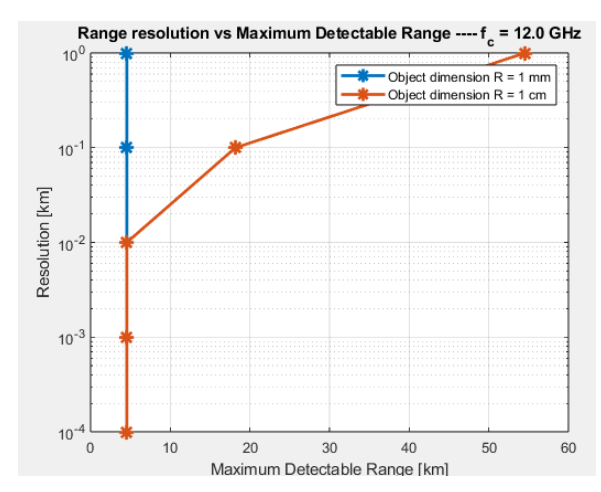
(b) Received Power vs Altitude - Tx: $IRIS^2$ -like high orbit / Rx: $IRIS^2$ -like low orbit @ $f_c = 12$ GHz

Figure 3.27: Received power vs altitude for two carrier frequencies.

detected even with the lowest bandwidth, while for 1-cm debris the $f_c = 12 \text{ GHz}$ performs slightly better but always for low value of Bandwidth.

In this case the detection of 1-mm debris is not possible, while for those of 1-cm is only possible from a Bandwidth $B=1.5~\mathrm{MHz}$ or lower. Here the statements done already for the monostatic case hold, since the detection can be done only with high value of Range Resolution, making the detection not reliable. The solution where the $IRIS^2$ -like constellation was used stand-alone to do the detection is not possible for both monostatic and bistatic case.





- (a) Range Resolution vs Maximum Detectable Range @ $f_c = 20 \text{ GHz}$
- (b) Range Resolution vs Maximum Detectable Range @ $f_c = 12 \text{ GHz}$

Figure 3.28: Comparison of range resolution vs maximum detectable range at different carrier frequencies.

3.5.2 $MetOp - SG : TX - IRIS^2(loworbit) : RX$

In this configuration the METOP-SG scatterometer, placed at orbit of 835 km, transmits the Radar signal, while an antenna placed above the $IRIS^2$ capture the backscattered signal from the debris from a lower orbit (750 km).

Parameters and Results

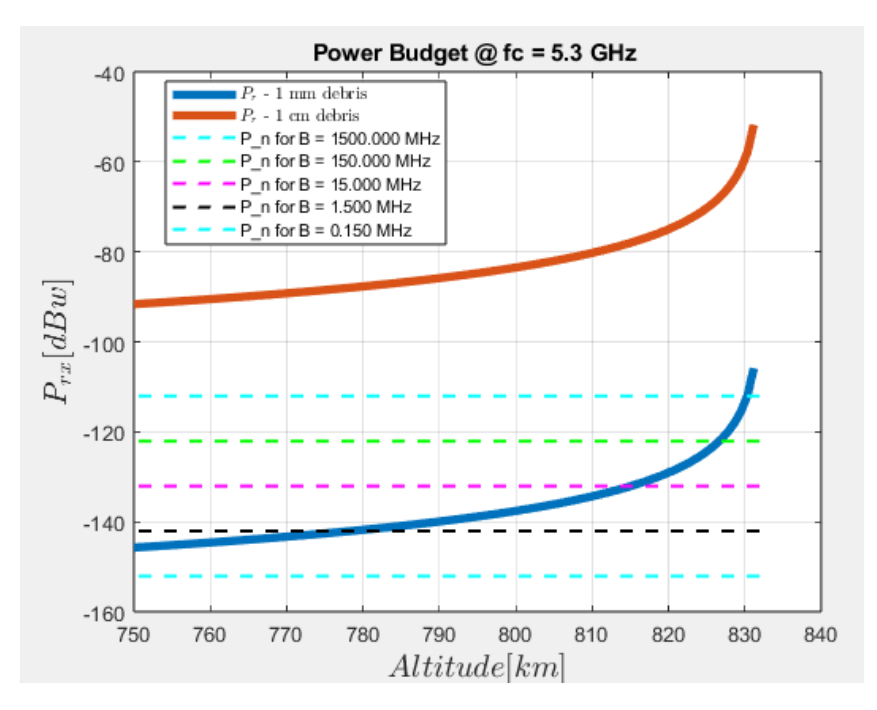


Figure 3.29: Received Power vs Altitude - Tx: METOP - SG / Rx: $IRIS^2$ -like low orbit

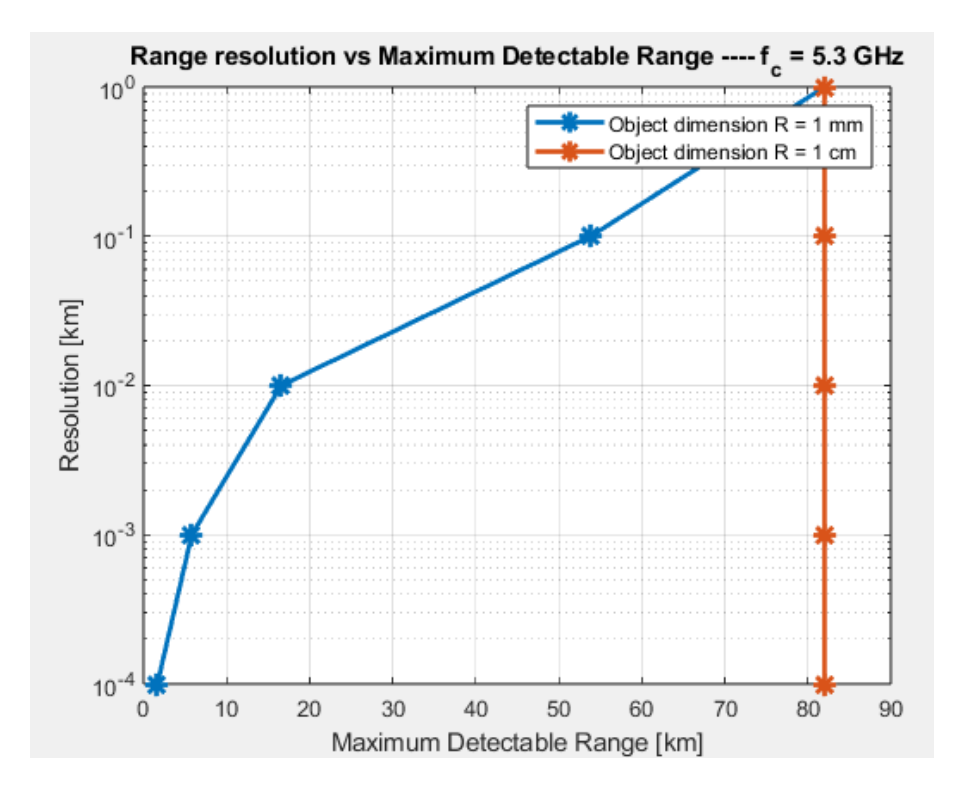


Figure 3.30: Range Resolution vs Detection Range Limit

Metop-SG had the highest performance, in this case we can observe that for :

- 1-cm debris results, it is able to detect the debris even with $\Delta R = 0.1$ m, lowest considered Range Resolution, the distance limit is given by the physical distance from the two constellation.
- 1-mm debris results, it is abble to cover the full distance between the two satellites only with high value of ΔR , which is too high w.r.t. the debris size

3.5.3 $HY2: TX - IRIS^2(loworbit): RX$

In this configuration the HY2 scatterometer, placed at orbit of 937 km, transmits the Radar signal, while an antenna placed above the $IRIS^2$ capture the backscattered signal from the debris from a lower orbit (750 km).

Parameters and Results



Figure 3.31: Received Power vs Altitude - Tx: HY2 / Rx: $IRIS^2$ -like low orbit

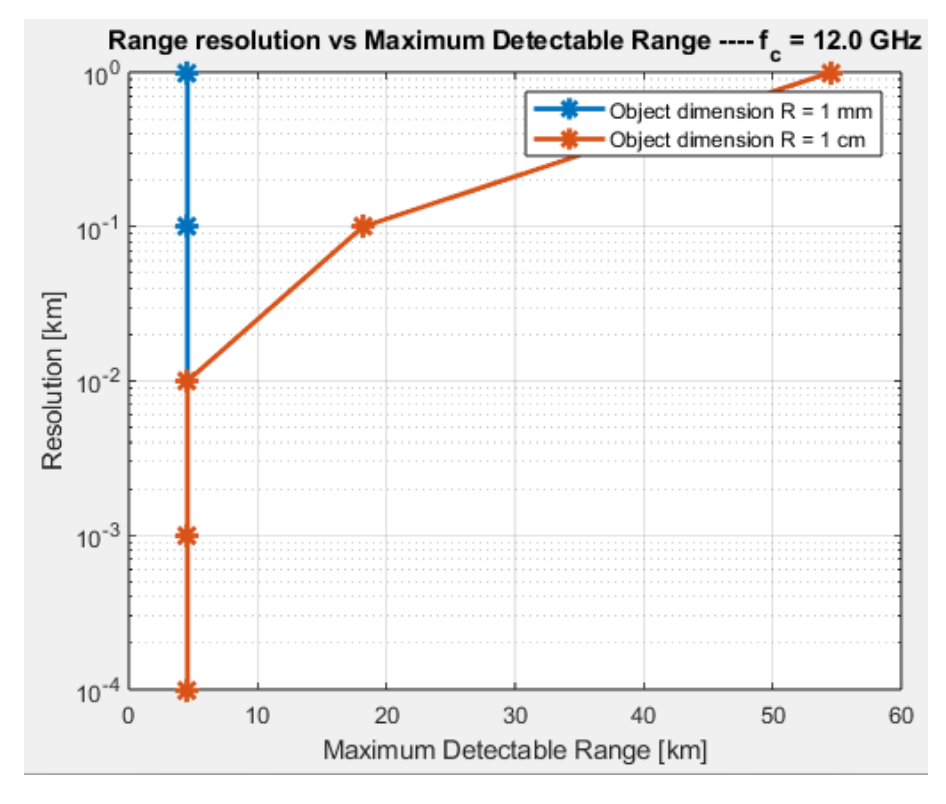


Figure 3.32: Range Resolution vs Detection Range Limit

As the results of the bistatic setup of $IRIS^2$ -like constellation, even in this case 1-mm debris cannot be detected to the low value of received power compared to the Noise Power, while for 1-cm the detection can be done only for high value of ΔR so the same consideration done before hold.

$\textbf{3.5.4} \quad TIRA: TX - IRIS^2(highorbit): RX$

Since TIRA is a ground RADAR and has high detection capabilities already in monostatic setup with bistatic being as close to the Region of interest, high density debris zone, as possible should increase the performance, in fact the reason why $IRIS^2$ -like satellites at high orbit , 1200 km , are considered is due to the fact that those in lower altitude don't reach physically our Region of interest.

Parameters and Results

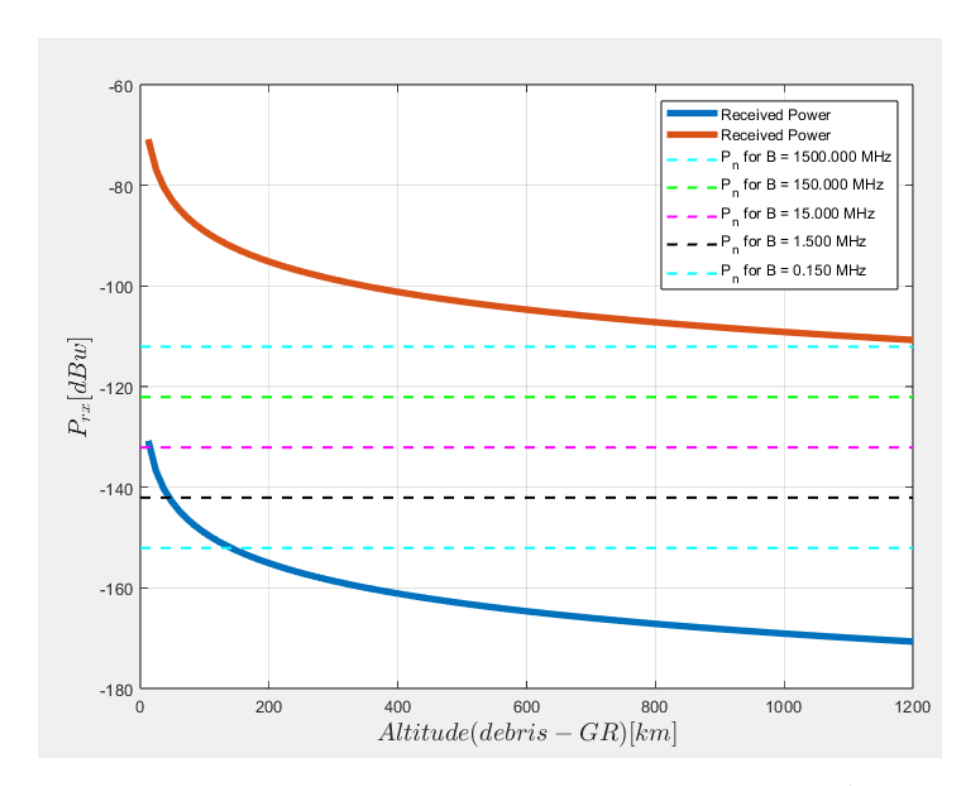


Figure 3.33: Received Power vs Altitude - Tx: TIRA / Rx: $IRIS^2$ -like high orbit

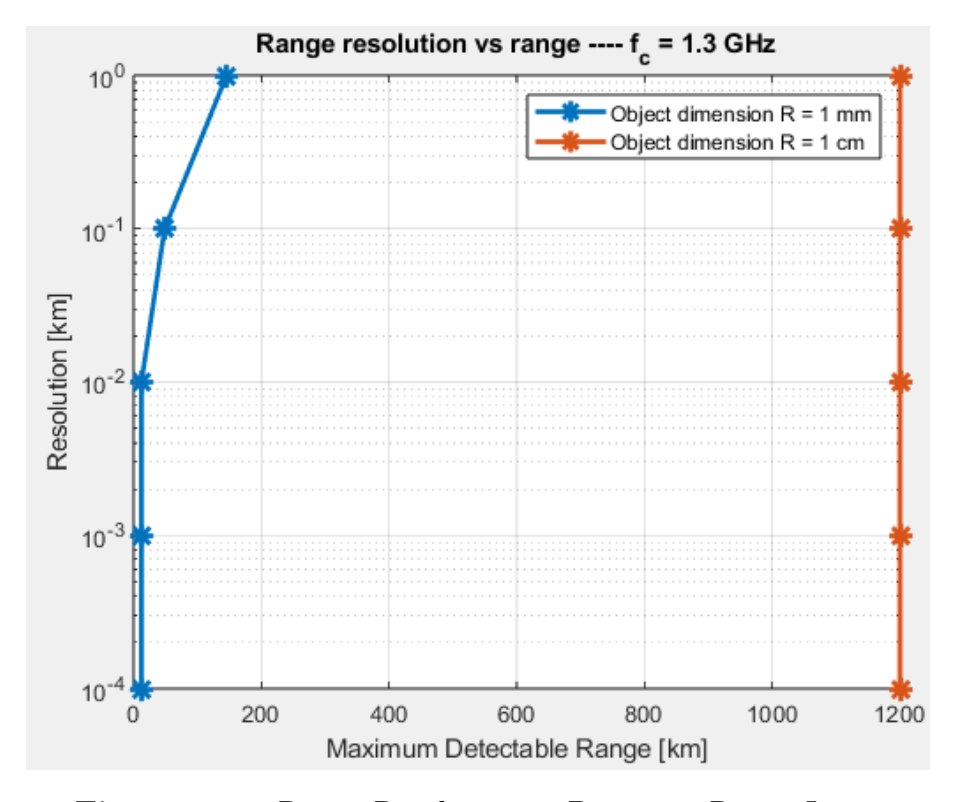


Figure 3.34: Range Resolution vs Detection Range Limit

TIRA, from the results shown in fig. 3.33 & 3.34, exploit a full coverage detection for 1-cm debris while for 1-mm debris is very limited, this is mostly due to the contribute

of the low frequency that lead to the lowest value considered for the RADAR CROSS SECTION.

$\textbf{3.5.5} \quad HUSIR: TX-IRIS^2(highorbit): RX$

The consideration made for TIRA ground RADAR holds, so $IRIS^2$ -like satellites at high orbit are considered and an antenna working at the carrier frequency of HUSIR is assumed to be used.

Parameters and Results

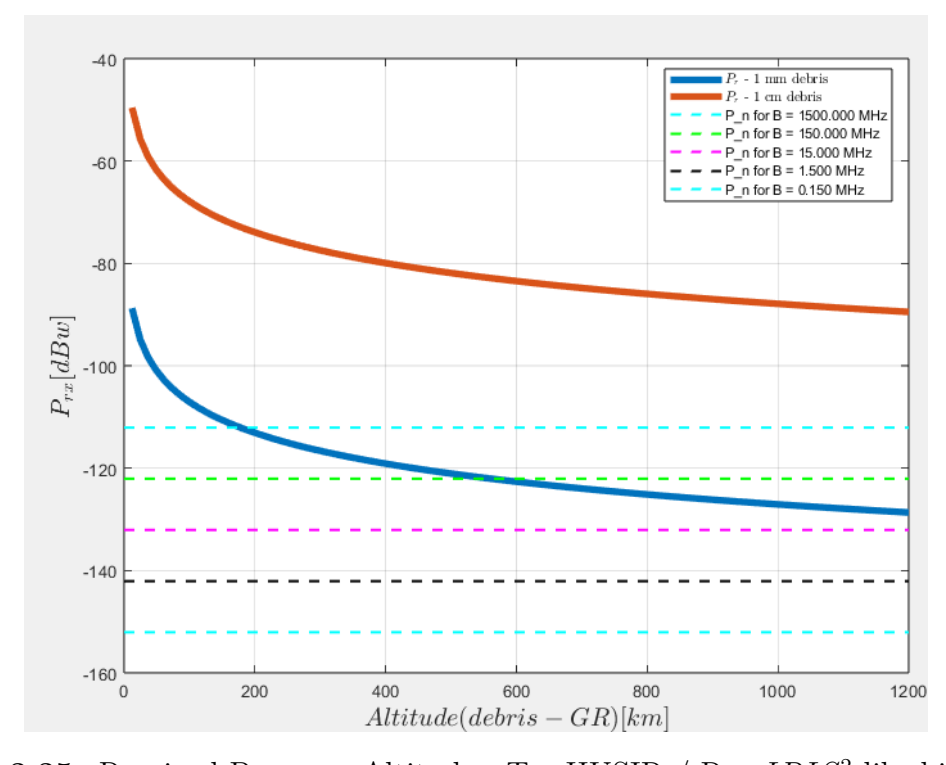


Figure 3.35: Received Power vs Altitude - Tx: HUSIR / Rx: $IRIS^2$ -like high orbit

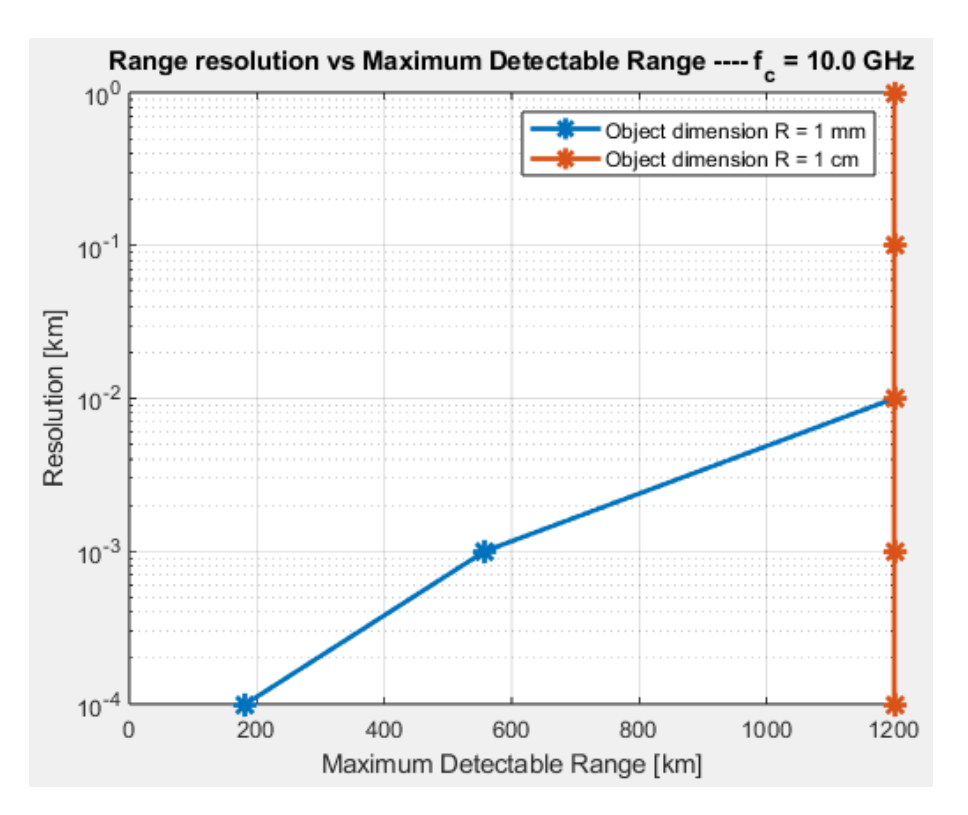


Figure 3.36: Range Resolution vs Maximum Detectable Range

As for TIRA, HUSIR show a full coverage for 1-cm debris, but here for 1-mm debris we can observe that already for $\Delta R = 10^{-2}$ km the detection over the full range is possible, untill now this is the best result obtained for all the type of setup, monstatic or bistatic, and combination of sat/ground radar.

3.6 Results comparison

After evaluating each of the possible combination, a general overview of the different systems capability w.r.t to the altitude can help better understand the previews results, since what has been shown untill now is each system MaximumDetectaleRange vs RangeResolution, so next step is to group all the results together and show the MDR vs Altitude, for the debris sizes.

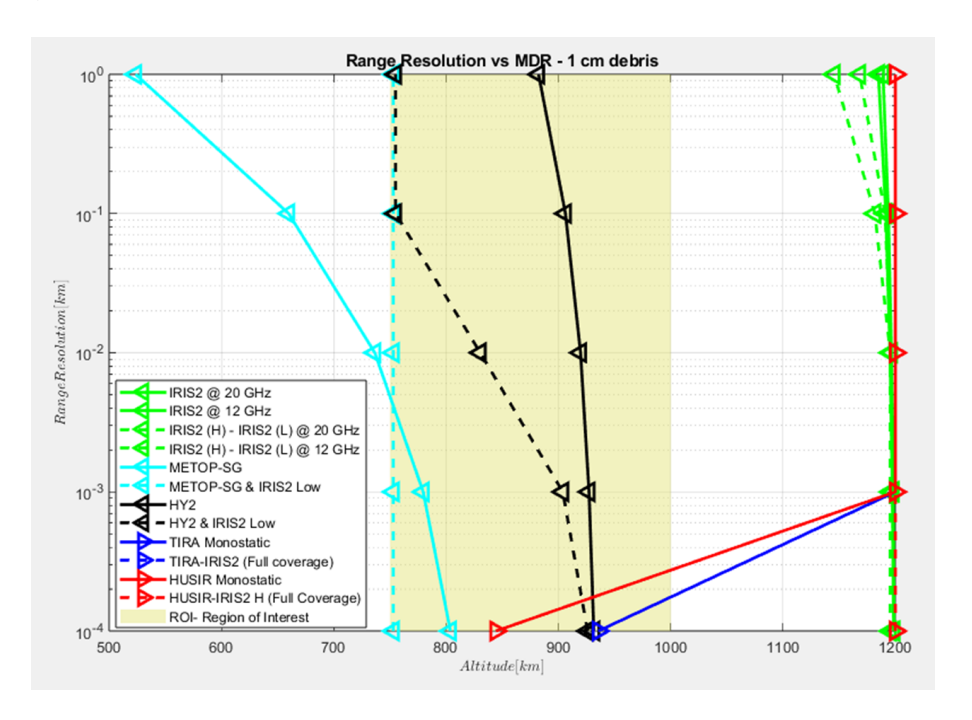


Figure 3.37: MDR vs Altitude - 1 cm

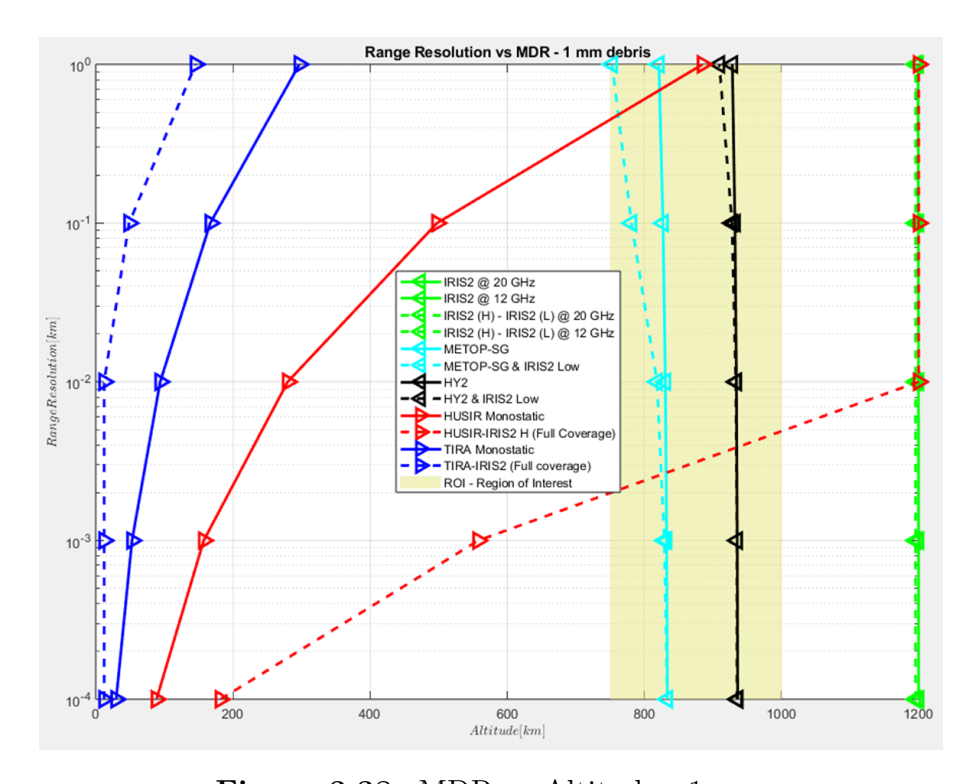


Figure 3.38: MDR vs Altitude - 1 mm

Now it can be more clear what are the combination that could detect debris at the region of interest, and those that are not able to reach those distances, obviously the benchmark is given by the ground Radar that have an higher transmitting power, P_t , while the satellite solution can provide only few **km** of coverage so those that are placed inside the ROI are more likely to provide a good detection with respect to those that are placed out. The fig. 3.37 and 3.38 show the results grouped together but one of the most important thing to take into account is the Bandwidth of each system, in fact the results where the ΔR , Range Resolution, is higher than the MDR, Maximum Detectable Range, are reasonable to be wiped out from the solution, since detecting small object with high Range Resolution means not being able to distinguish many object that are near. So we can remove them from the analysis and hold only those for which the $MDR \geq \Delta R$, or those that at least can detect inside the Region of Interest.

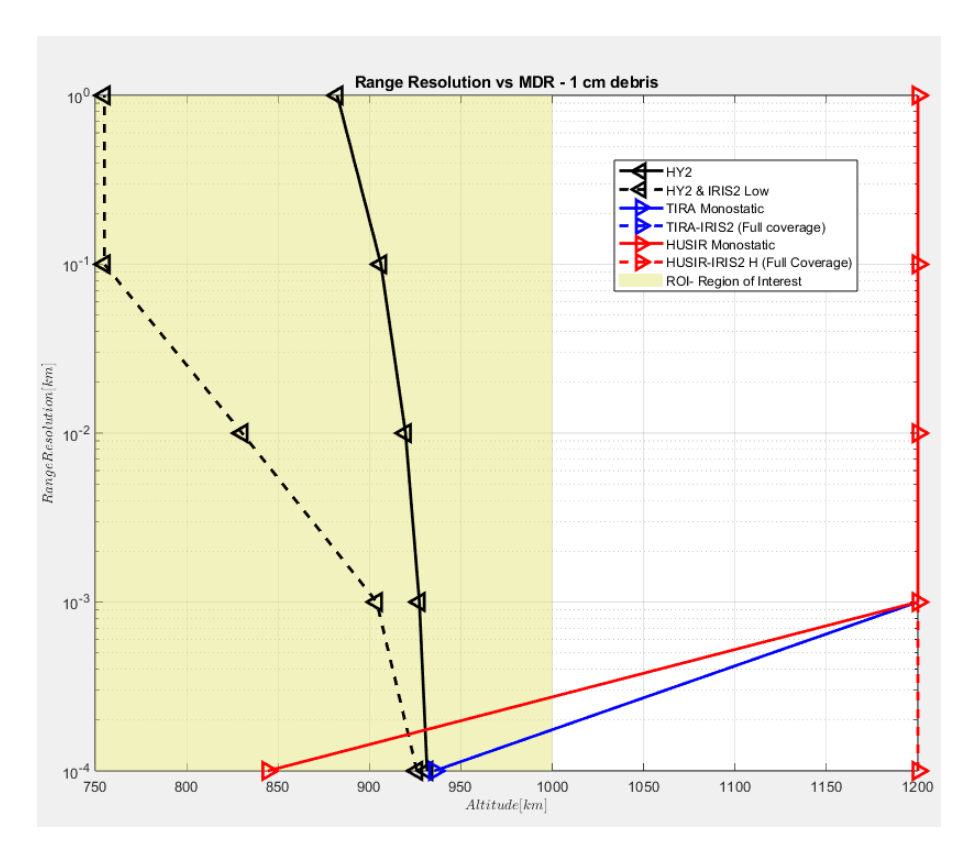


Figure 3.39: MDR vs Altitude, only the valuable results kept - 1 cm debris

Starting from the result for 1-cm debris size, the following solutions were kept:

- HY-2, in both monostatic and bistatic setup, even if the bibstatic has an higher coverage at equal Range Resolution ΔR , in this case it perfectly works inside the Region of interest and even if the detection with low ΔR is limited, it can give a complementary detection with the others.
- TIRA and HUSIR, as expected are those with the highest performance and it increase if the detection is done at RX side, the provide a full detection already with $\Delta R = 10^{-3}$ km.

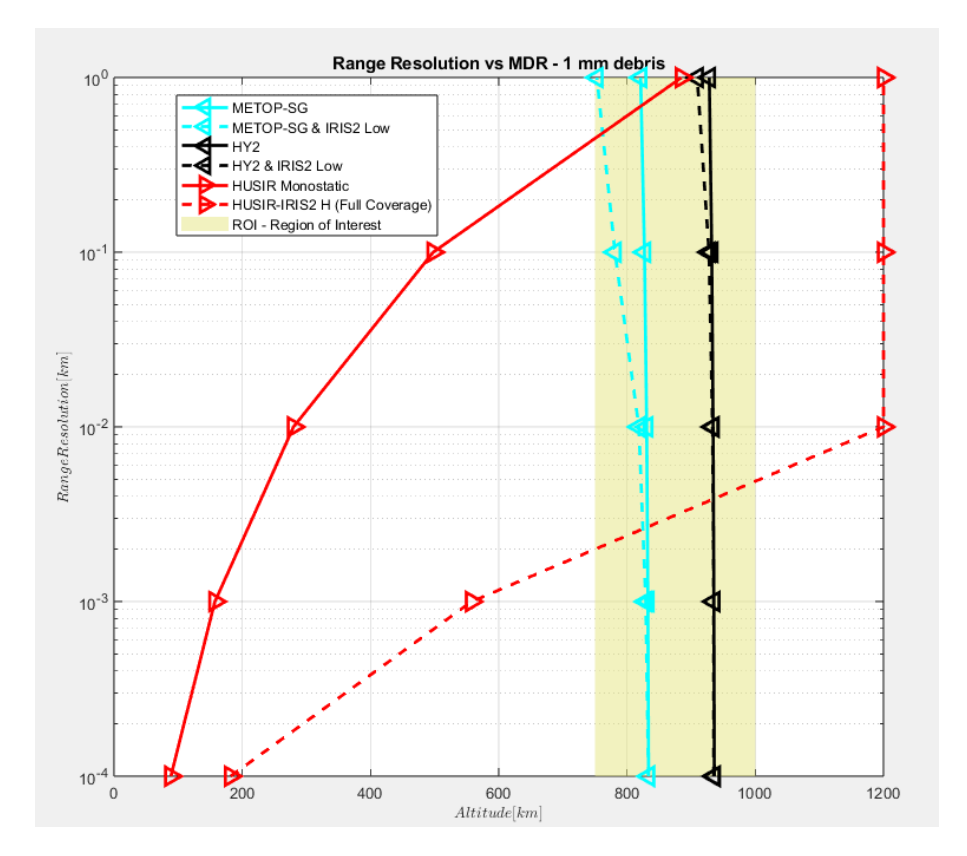


Figure 3.40: MDR vs Altitude, only the valuable results kept - 1 mm debris

The rational behind the kept results for 1-mm debris size is the basically the same as the one presented before in fig. 3.39. An overall consideration that now is clear is that the Setup HUSIR as TX and $IRIS^2 - like$ in high orbit is the most performing, providing detection with low ΔR for 1 - cm debris and an optimal solution for 1-mm debris too. So now we can focus on this solution and try to give an idea on how to improve the system detectability performance.

3.6.1 Optimization

In order to try to improve the detection of 1-mm debris, since are those for which the ΔR is still high for the detection, it is possible to think of a redesign of the system, and if we would change only a parameter it would be something related to the RCS, this term is not directly connected to the characteristic of the system that is used but it depends, as we have seen in the previous paragraph, to the central frequency used. HUSIR is known to use the X-Band, so around $f_c = 10$ GHz, now by focusing on the fig. 3.41, we can say that most of the band that we've analyzed so far are inside the Rayleagh Region for which the increase is exponential in the first trait and diminsh its behavior when the $r \simeq \lambda$, where r is the radius and λ is the wavelength. This mean that by using an higher frequency the contribution given by the RCS should increase, but something to highlight is the following, let's focus on the Received Power formula P_r :

$$P_r = \frac{P_{\text{tx}} \cdot G_{\text{tx}} \cdot Code_{en} \cdot G_{\text{rx}} \cdot \lambda^2 \cdot \sigma}{(4\pi)^3 \cdot d^4}$$
(3.14)

In the formula we have two parameters that depends on the f_c that are :

1.
$$\sigma = 9\pi r^2 (kr)^4$$
, $r \ll \lambda$

2.
$$\lambda = \frac{c}{f_c}$$

this lead to have an attenuation from the λ^2 factor and an contribution for what concern σ .

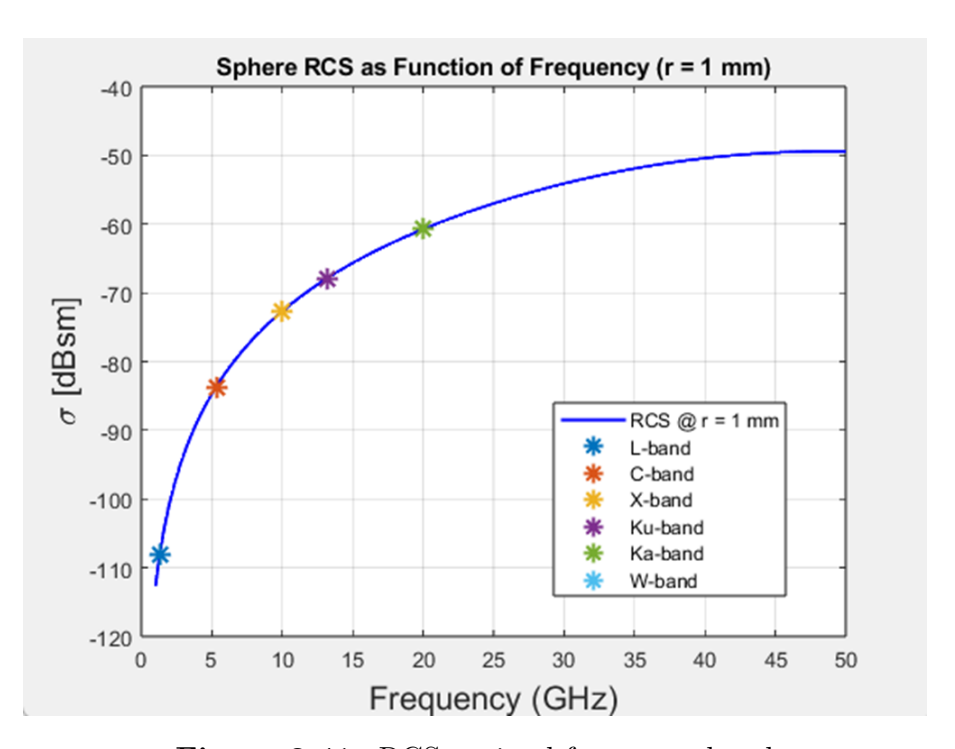


Figure 3.41: RCS optimal frequency band

in fig.3.3, the Ka-band is the one considered in this analysis for which the value of the RCS is the highest, since we have not considered the optimal solution for the overall RCS behavior. Now assuming that the HUSIR could work at $f_C = 20$ **GHz**,we analyze the impact of the frequency on the detection capability of the system.

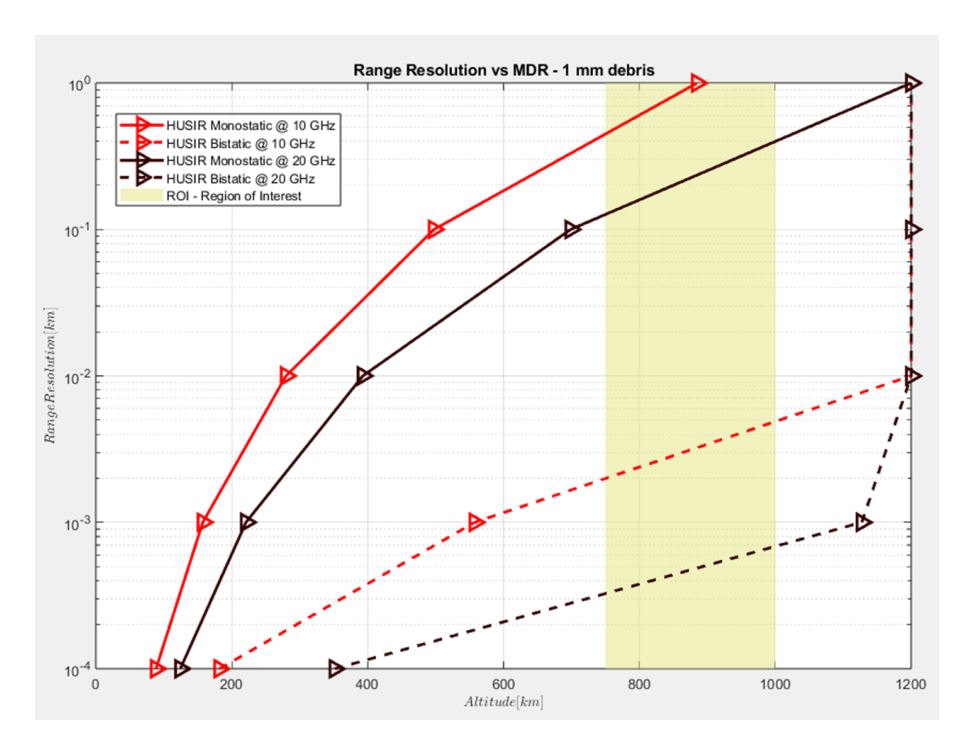


Figure 3.42: Range Resolution vs MDR, HUSIR @ 10 GHz(RED) / HUSIR @ 20 GHz (Brown)

From fig. 3.42, we can observe that the HUSIR working at @ 20 (brown) **GHz**, has some gain for both the setup, the highest improvement is for $\Delta R = 10^{-3}$ **Km**, for which the bistatic setup (dashed brown line) obtain an improvement of detection from 500 **km** to around 1100 **km**.

Chapter 4

Conclusion

The primary focus of this thesis was to provide an overview of potential solutions for detecting LNT(Lethal Non Trackable) debris, in the first part of the research a JCAS(Joint Communication and sensing) system has been studied in order to understand if the sensing of those debris was possible through the newly $IRIS^2$ constellation, that has to be deployed in the future. After analyzing the first results it was clear that for the scope meant into this thesis, this approach needs some improvement in the overall system capability. So after, some of the already deployed constellation and Ground Radar haven been chosen in order to understand if the available resources could reach the scope. After analyzing all the possible configuration, leaving $IRIS^2$ as the main constellation to be used in bistatic cases such that an higher degree of freedom was possible, the configuration that shown the highest performance was HUSIR in monostatic configuration or better Bistatic, after obtaining those results an optimization based on the RCS analysis has been proposed to enhance the detection capability of the system.

To enhance the overall study and achieve more reliable results, certain approximations needs further investigation. The first area for improvement is the Radar Cross Section (RCS). Approximating debris as spheres is a simplification; while characterizing the real shape of debris may be time-consuming, a more nuanced approach could yield better results. For instance, analyzing a variety of known basic shapes and averaging the results could provide a more accurate model.

The idea behind the thesis is to give an overview of the current

In summary, two main conclusions can be drawn. First, the objective was to design a system to aid in cataloging space debris, particularly in high-density zones. The goal was to identify a system capable of reaching the region of interest with an optimal trade-off between the Maximum Detectable Range and the Range Resolution. For this challenge, the combination of HUSIR as the transmitter and an IRIS²-like satellite constellation as the receiver demonstrated the best performance. This configuration can detect 1-cm debris across all high-density zones, even with a low Range Resolution. For 1-mm debris, the required Range Resolution is slightly higher but remains within an acceptable range.

Finally, it is important to note that the debris problem can be addressed not only through long-distance detection and tracking with high bandwidth but also by mitigating the hazard to satellites themselves. In a collision avoidance scenario, even solutions previously deemed unsuitable for detection may become viable.

Bibliography

- [1] HDI Global Specialty SE. Space Debris Technical Study. 2023. URL: https://www.hdi-specialty.com/(cit. on pp. 1, 2, 4).
- [2] R. Buchs. Collision risk from space debris: Current status, challenges and response strategies. Tech. rep. Lausanne: EPFL International Risk Governance Center, 2021 (cit. on p. 2).
- [3] ESA. Space debris by the numbers. [Accessed 28 March 2022]. Mar. 2022. URL: https://www.esa.int/Safety_Security/Space_Debris/Space_debris_by_the_numbers (cit. on p. 3).
- [4] T. Maclay and D. McKnight. «Space Environment Management: Framing the Objective and Setting Priorities for Controlling Orbital Debris Risk». In: 70th International Astronautical Congress (IAC). Washington D.C., 2019 (cit. on p. 3).
- [5] Francesco Tonon et al. «Crowded Space: A Review on Radar Measurements for Space Debris Monitoring and Tracking». In: *Applied Sciences* 11.4 (2021), p. 1364. DOI: 10.3390/app11041364. URL: https://www.mdpi.com/2076-3417/11/4/1364 (cit. on pp. 5, 6).
- [6] European Space Agency (ESA). Space Debris Mitigation Handbook. https://www.esa.int/Safety_Security/Space_Debris. 2019 (cit. on p. 5).
- [7] NASA. NASA-STD-8719.14B: Process for Limiting Orbital Debris. https://standards.nasa.gov/. 2019 (cit. on p. 5).
- [8] Francesco Tonon et al. «Crowded Space: A Review on Radar Measurements for Space Debris Monitoring and Tracking». In: *Applied Sciences* 11.4 (2021), p. 1364. DOI: 10.3390/app11041364. URL: https://www.mdpi.com/2076-3417/11/4/1364 (cit. on p. 5).
- [9] Yuan Liu, M. R. Bhavani Shankar, Linlong Wu, and Björn Ottersten. «Debris Sensing Based on LEO Constellation: An Intersatellite Channel Parameter Estimation Approach». In: *Proceedings of the IEEE International Conference on Acoustics, Speech and Signal Processing (ICASSP)*. IEEE, 2024, pp. 1–5. DOI: 10.1109/ICASSP48485.2024.10446432 (cit. on p. 7).
- [10] Yoshinori Arimoto, Junzo Uchida, and Anastasia Semerok. «Space Debris Detection Using Laser Communications Demonstration Equipment». In: *Proceedings of the IEEE*. Available via IEEE Xplore. IEEE, 2000. URL: https://ieeexplore.ieee.org/document/58465 (cit. on pp. 13–15).
- [11] Siyeon Park. Europe signs contracts for IRIS² constellation. Accessed: 2025-06-16. 2024. URL: https://spacenews.com/europe-signs-contracts-for-iris%C2% B2-constellation/ (cit. on pp. 28, 45).

- [12] European Space Agency ESTEC. Demonstrator of a Transmit Dual Polarised Active Antenna with Large Scan Angle for Low Earth Orbit Applications. Tender documentation. Tender no.1-11232 (ARTES5B.216), pubblicato 2 febbraio 2022. Feb. 2022. URL: https://www.developmentaid.org/tenders/view/924446/demonstrator-of-a-transmit-dual-polarised-active-antenna-with-large-scan-angle-for-low-earth-orbit-applications/ (cit. on pp. 28, 45).
- [13] World Meteorological Organization (WMO). SCA (Scatterometer) instrument details. https://space.oscar.wmo.int/instruments/view/sca_scatterometer. [Accessed: 17 June 2025]. 2025 (cit. on p. 31).
- [14] eoPortal / ESA. MetOp Space and Hardware Components. https://www.eoportal.org/satellite-missions/metop#space-and-hardware-components. [Accessed: 17 June 2025]. 2025 (cit. on pp. 31, 33).
- [15] World Meteorological Organization. HY-2B (Hai Yang 2B) Observing Systems Capability Analysis and Review Tool. https://space.oscar.wmo.int/satellites/view/hy_2b. Última actualización 9 enero 2025, acceso 19 junio 2025. 2025 (cit. on p. 34).
- [16] An Liu. A Follow-on for the Scatterometers Onboard the Chinese HY-2 Satellites Series-1. Technical Report. Accedido el 19 de junio de 2025. Florida State University / COAPS Meeting, Nov. 2023 (cit. on p. 34).
- [17] Fraunhofer Institute for High Frequency Physics and Radar Techniques (FHR). Space observation radar TIRA Technical Equipment. https://www.fhr.fraunhofer.de/en/the-institute/technical-equipment/Space-observation-radar-TIRA.html. Accessed on 19 June 2025; describes a 34m parabolic antenna under a 47.5 m radome, operable in L-band (1.333 GHz) and Ku-band (16.7 GHz):contentReference[oaicite:0]index=0. 2025 (cit. on p. 36).
- [18] J. Murray, C. Blackwell, J. Gaynor, and T. Kennedy. Haystack Ultra-Wideband Satellite Imaging Radar Measurements of the Orbital Debris Environment: 2014-2017. Tech. rep. NASA/TP-2019-220302. Accessed: 2025-06-19. NASA Johnson Space Center, 2019. URL: https://ntrs.nasa.gov/api/citations/20190028719/downloads/20190028719.pdf (cit. on p. 38).